An Analysis of the Unmanned Aerial Systems-to-Ground Channel and Joint Sensing and Communications Systems Using Software Defined Radio

by

Richard M. Gutierrez

A Dissertation Presented in Partial Fulfillment
of the Requirements for the Degree
Doctor of Philosophy

Approved April 2018 by the
Graduate Supervisory Committee:

Daniel W. Bliss, Chair
Antonia Papandreou-Suppappola
Umit Ogras
Cihan Tepedelenlioglu

ARIZONA STATE UNIVERSITY

May 2018

ABSTRACT

Software-defined radio provides users with a low-cost and flexible platform for implementing and studying advanced communications and remote sensing applications. Two such applications include unmanned aerial system-to-ground communications channel and joint sensing and communication systems. In this work, these applications are studied.

In the first part, unmanned aerial system-to-ground communications channel models are derived from empirical data collected from software-defined radio transceivers in residential and mountainous desert environments using a small (<20 kg) unmanned aerial system during low-altitude flight (<130 m). The Kullback-Leibler divergence measure was employed to characterize model mismatch from the empirical data. Using this measure the derived models accurately describe the underlying data.

In the second part, an experimental joint sensing and communications system is implemented using a network of software-defined radio transceivers. A novel co-design receiver architecture is presented and demonstrated within a three-node joint multiple access system topology consisting of an independent radar and communications transmitter along with a joint radar and communications receiver. The receiver tracks an emulated target moving along a predefined path and simultaneously decodes a communications message. Experimental system performance bounds are characterized jointly using the communications channel capacity and novel estimation information rate.

DEDICATION

For my mother, Darlene, and my father, Manuel Jr., who instilled in me the value of love, hard work, dedication and the value of an education. For my grand parents, Vernon, Norma, Manuel Sr. and Beatrice, whose love and sacrifice remain dear to my heart and will never be forgotten. For my Uncle Micael whose advice and constant encouragement helped me to get this far. For my brother, Israel, whose perseverance through adversity has taught me to never give up on pursuing my dreams. For my family and friends, whose love, support and guidance throughout my life has helped shape the person I am today. For my wife, Stephanie, who helped to keep me motivated and focused through both the highs and lows of my graduate career. Lastly, I dedicate this thesis to any person who has dreams and pursues them to the fullest, embracing every obstacle and pushing themselves beyond their limits to discover their full potential.

ACKNOWLEDGMENTS

I first wish to acknowledge my graduate advisor and mentor Professor Dan Bliss. His guidance and assistance in the course of this research was invaluable and extended far beyond the classroom. Over the four years that I have known and worked with him, he has shared his ideas, time, resources, and monetary support graciously with me. For this, I am most appreciative.

I would like to acknowledge my fellow colleagues and co-authors who donated their time reviewing my work and providing feedback, including Alex R. Chiriyath, Hanguang Yu, Yu Rong, Wylie Standage-Beier, Andrew Herschfelt, Arindam Dutta, and Gerard Gubash.

Additionally, I would like to acknowledge Professors Antonia Papandreou-Suppappola, Umit Ogras, and Cihan Tepedelenlioglu for their time in reviewing early drafts of this work and for serving on my examination committee. I would like to also acknowledge the many professors who contributed to my graduate education at Arizona State University (ASU). Their personalized attention and dedication to the students of the department helped me to be successful.

Finally, I would like to acknowledge the various sponsors who provided funding for this research including the Massachusetts Institute of Technology Lincoln Laboratory (MIT/LL), the Office of Naval Research (ONR) and Raytheon BBN Technologies. I would also like to acknowledge ASU for their support through the Dean's Fellowship. Further I would like to acknowledge The National Graduate Education for Minorities (GEM) Consortium and The Johns Hopkins University Applied Physics Laboratory (JHU/APL) for their support through a full GEM fellowship.

TABLE OF CONTENTS

CHAPTER Page

CHAPTER Page

LIST OF FIGURES

Figure Page

LIST OF TABLES

Chapter 1

INTRODUCTION

1.1 Background

Software-defined radio (SDR) is a widely used radio technology because of its affordability, flexibility and portability. Unlike traditional radios, whose components are implemented in hardware, SDRs are typically implemented through the use of software or re-definable logic. Typically, this is accomplished using small, low-power, and low-cost digital components, such as a general purpose digital signal processor or field-programmable gate array. As a result, SDR is an ideal candidate for multi-carrier, single-carrier, single-band, multi-band, or multi-mode transceiver systems. The SDR has the ability to change modes arbitrarily and navigate a wide range of frequencies with programmable channel bandwidth, data rate, conversion gain, and modulation characteristics. The SDR has helped pave the way for users to implement advanced communications and sensing systems across a multitude of application areas.

One of these application areas is unmanned aerial system (UAS) communications and is currently a thriving area of research. The study of UAS communications can be grouped broadly into three application areas: UAS-aided ubiquitous coverage, UAS-aided relaying, and UAS-aided information dissemination and data collection [1]. In the UAS-aided ubiquitous coverage scenario, UASs are deployed to assist with pre-existing or non-existent communications infrastructure. In the UAS-aided relaying scenario, UASs are deployed to provide a line-of-sight (LoS) communications link between users. Finally, in the UAS-aided information and dissemination scenario,

UASs are deployed to collect or disseminate information to a collection of ground sensors. In each of these application areas, the characterization and modeling of the UAS air-to-ground multipath propagation for different environments is vital for optimal system performance.

Another state-of-the-art application area that utilizes SDR technology is joint radar and communications or more broadly, joint sensing and communications. Joint sensing and communications systems attempt to address the growing problem of spectral congestion, where multiple users compete for finite radio frequency (RF) spectral resources. A joint sensing and communications system incorporates a co-design architecture in which radar and communications functions are designed to cooperate. Such an architecture is feasible and can be implemented using the SDR platform. This paradigm shift towards designing systems to operate jointly within a given bandwidth allocation with mutual benefit is referred to as radio frequency (RF) convergence for sensing and communications [2, 3]. The RF convergence concept represents a solution that promises mutually increased performance for both remote sensing and communications systems.

1.2 Literature Survey

1.2.1 Software Defined Radio

During the 1970s, implementations of digital radios emerged whose baseband processing was implemented in software. For example, very low frequency (VLF) radios were constructed using the Intel 8085 microprocessor to perform baseband processing [4]. The term "software radio" was introduced in a 1985 E-Systems (now Raytheon) company newsletter to describe a prototype digital baseband receiver developed in their Space Systems Department [5]. The first major developments for the software

radio was The Defense Advanced Research Projects Agency (DARPA) SPEAKeasy system [6].

In 1992, Joseph Mitola published the first article discussing the software radio architecture and the required hardware performance needed to implement such a system [7]. The first industry associated forum dedicated solely to software radio was established in 1996 as "The Modular Multifunction Information Transfer System (MMITS) Forum." It was at this forum that the term "Software Defined Radio" was adopted as the industry standard. In 2004, Vanu Inc. received the first commercial approval from the Federal Communications Commission (FCC). This paved way for a wide variety of low-cost SDRs to become commercially available including Ettus Research Universal Software Radio Peripheral (USRP), Great Scott Gadgets HackRF One, and Lime Microsystem's LimeSDR.

1.2.2 UAS-to-Ground Channel Modeling

Reference [8] possibly represents the earliest example of modeling the air-to-ground channel using empirical data. In their work, Dyer et al. gathered measurements in the Very High Frequency (VHF) band with a signal bandwidth of approximately 5 MHz. Using these measurements the authors generate a channel model for both fading and time dispersion for use in air traffic control applications. Early experiments utilizing commercially available small UAS, utilized IEEE 802.11 wireless local area network (Wi-Fi) technology to study received signal strength and User Datagram Protocol (UDP) throughput in air-to-ground links [9–11].

More recent stochastic modeling of the low-altitude UAS channel from ultra-wideband (UWB) empirical measurements using a Tarot 650 quadcopter was conducted in Reference [12]. Additional stochastic characterizations and modeling of the UAS channel were reported in References [13] and [14] for a semi-urban environment

using measurements from a hexacopter. Further stochastic characterizations of the UAS channel in residential and mountainous desert environments were reported in Reference [15]. Finally, micro-Doppler measurements of the UAS utilized in Reference [15] were studied in Reference [16].

1.2.3 Joint Sensing and Communications Systems

Historically, traditional communications and sensing systems are designed in isolation, treating each other as interference in the design process. Within this framework, modern approaches to addressing spectral congestion have looked at waveform design to provide a potential solution. Researchers have considered a variety of waveform options including orthogonal frequency-division multiplexing (OFDM) [17–20]. Similar to OFDM, spread spectrum waveforms have been proposed for their attractive, noise-like autocorrelation properties [21–23].

MIMO radar techniques have been suggested, given that the independent transmitted waveforms allow more degrees of freedom for joint radar-communications co-design [24–26]. Multiple orthogonal linear frequency modulated chirps have also been proposed to accomplish both radar detection and communications transmissions in a MIMO system [27]. Researchers have also looked at optimization theory based radar waveform design methods in spectrally dense environments that attempt to maximize some radar performance metrics (detection probability, ambiguity function features etc.) while keeping interference to other in-band systems at a minimum [28–30].

Researchers have searched several other research areas for potential solutions to the spectral congestion problem. Some researchers looked at spatial mitigation as a means to improve spectral interoperability [31–33]. Joint coding techniques, such as robust codes for communications that have desirable radar ambiguity properties, as

well as codes that trade data rate and channel estimation error have been investigated as co-design solutions [34–36].

Many modern applications have transitioned from the above classical design approaches to co-designed, joint sensing and communications systems. In the co-design process, both radar and communications functions are developed and optimized jointly to benefit from the presence of each other. The new paradigm shift towards co-designing systems to achieve sensing and communications convergence (RF convergence for short) has broad applicability across a multitude of application areas. To name a few, Li-Fi, Lidar, commercial flight control, communications and military radar [3] can all benefit from a co-designed architecture.

During the co-design process it is important to have established metrics and bounds to understand system performance. The information rate capacity derived by Shannon in [37] is a well established metric for characterizing communications systems performance. Recently, a novel metric, the estimation information rate, was introduced by Bliss in Reference [38] to characterize radar target delay tracking performance. The estimation rate was then extended to include Doppler estimation within the Kalman filter framework in Reference [39]. These metrics are utilized to characterize joint sensing and communications system performance in a similar fashion as the traditional multiple access performance bounds.

In subsequent publications, Chiriyath et. al. derived bounds in terms of the aforementioned metrics for the multiple access topology [2]. Additional publications investigated the effect of continuous waveform optimization on these bounds [40], as well as the impact of clutter and phase noise [41]. Further bounds for multiple antenna systems were derived in Reference [42]. Until recently, these bounds have only been investigated in simulation. However, a new SDR network [43] provides an easy to use developmental environment to implement the necessary algorithms to

explore these bounds experimentally. A demonstration of the feasibility of a co-design architecture using this network was implemented in Reference [44]. Subsequently, an initial investigation of these bounds was conducted in Reference [45] using the same network.

1.3 Contributions

This work and corresponding publications will focus on studying two specific areas: the unmanned aerial system (UAS)-to-ground communications channel and joint sensing-communications performance bounds. In particular, the focus will be on studying these areas through the use of SDR. In terms of the UAS-to-ground communications channel, the following contributions will be made:

1. Discuss channel sounding experiments conducted in residential and mountainous desert terrains utilizing commercially available SDR and small UAS (less than 20 kg) in low altitude settings (less than 130 meters);

2. Study the time and frequency dispersion characteristics from the recorded measurements;

3. Construct channel models from these measurements.

4. Finally, discuss the performance of the channel models in terms of how accurately they describe the underlying measurement data.

Most work in modeling the UAS-to-ground channel focuses on regimes utilizing larger aircraft flying at much higher speeds. Current work using small low-altitude UAS to generate channel models from empirical data is scarce. The purpose of this work is to contribute to this area and provide useful channel models to aide system designers.

In terms of joint sensing and communications systems, this work will focus on developing a novel co-design architecture and experimentally generate performance bounds. The following contributions will be made:

1. Demonstrate an experimental joint sensing and communication multiple access system on a state-of-the-art SDR network, focusing on a co-designed receiver architecture;

2. Discuss the signal processing algorithms used within the receiver architecture;

3. Experimentally generate various bounds on the system performance including the multiple access channel bound, isolated sub-band bound, communications water-filling bound, and the successive interference cancellation bound.

As mentioned earlier, most work in this area has been through simulation and thus, this work is meant to be a point of origin for designing and implementing these systems in practice.

1.4 Notational and Mathematical Preliminaries

This section contains a number of useful definitions and relationships used throughout this text. In the remainder of the text, it is assumed that the reader has familiarity with these topics. Most of the notation used in this work is adapted from [46].

Table of Symbols

$a \in \mathbb{S}$	a is an element of the set $\mathbb{S}$
$\mathbf{A}^{\dagger}$	Hermitian conjugate of matrix $\mathbf{A}$
$\mathbf{A}^{T}$	Non-Hermitian transpose of matrix $\mathbf{A}$
$j = \sqrt{-1}$	Imaginary number

$\lfloor \cdot \rfloor$	Floor operation
$\lceil \cdot \rceil$	Ceil operation
$*$	Convolution operator
$\| \cdot \|$	L_2 Norm (vector) or absolute value (scalar)
$\odot$	Hadamard product for matrices and vectors

Scalars, Vectors, and Matrices

A scalar is denoted by a non-bold letter such as a or A. Scalars are integers ($\mathbb{Z}$), real ($\mathbb{R}$), or complex numbers ($\mathbb{C}$):

$$\begin{aligned} &a \in \mathbb{Z}, \\ &a \in \mathbb{R}, \text{or} \\ &a \in \mathbb{C}, \end{aligned} \tag{1.1}$$

respectively.

Vectors are denoted by a lowercase bold letter. For example, a column vector of N complex scalars is indicated by

$$\mathbf{a} \in \mathbb{C}^{N \times 1}. \tag{1.2}$$

Similarly, a row vector of N complex scalars is denoted by a lowercase bold letter with an underscore

$$\underline{\mathbf{a}} \in \mathbb{C}^{1 \times N}. \tag{1.3}$$

The n^{th} element of column vector $\mathbf{a}$ is denoted by

$$\{\mathbf{a}\}_n \quad \text{for} \quad n = 0, 1, \ldots, N-1. \tag{1.4}$$

The convolution of two vectors $\mathbf{a} \in \mathbb{C}^{N\times 1}$ and $\mathbf{h} \in \mathbb{C}^{M\times 1}$ is

$$\mathbf{s} = \mathbf{a} * \mathbf{h} \tag{1.5}$$

$$= \sum_{m=-M}^{M} \{\mathbf{a}\}_{n-m} \{\mathbf{h}\}_{m}, \tag{1.6}$$

where $\mathbf{s} \in \mathbb{C}^{N+M-1}$. The absolute value of a scalar or L_2 norm of vector is denoted by $\|\cdot\|$. The $L2$ norm of column vector $\mathbf{a}$ is [46]

$$\|\mathbf{a}\| = \sqrt{\mathbf{a}^{\dagger}\,\mathbf{a}} \tag{1.7}$$

$$= \sqrt{\sum_{n=0}^{N-1} \|\{\mathbf{a}\}_{n}\|^2}. \tag{1.8}$$

Matrices are denoted by bold uppercase letters. For example, a matrix consisting of $M \times N$ real elements is indicated by [46]

$$\mathbf{A} \in \mathbb{R}^{M\times N}. \tag{1.9}$$

The element of m^{th} row and n^{th} column of matrix $\mathbf{A}$ is indicated by

$$\{\mathbf{A}\}_{m,n} \tag{1.10}$$

The determinant of a square matrix $|\mathbf{A}|$ is given by [46]

$$|\mathbf{A}| = \sum_{n=0}^{N-1} \{\mathbf{A}\}_{m,n} (-1)^{m+n} |\mathbf{M}_{m,n}|, \tag{1.11}$$

where submatrix $\mathbf{M}_{m,n}$ is defined to be the minor of $\mathbf{A}$, which is constructed by removing the m^{th} and n^{th} column of $\mathbf{A}$. It is not to be confused with the m^{th} or n^{th} element of $\mathbf{A}$.

The Hadamard product is the elementwise multiplication of each value between two vectors or two matrices. For matrices $\mathbf{A} \in \mathbb{R}^{M\times N}$ and $\mathbf{B} \in \mathbb{R}^{M\times N}$

$$\mathbf{A} \odot \mathbf{B} = \{\mathbf{A}\}_{m,n} \{\mathbf{B}\}_{m,n}, \tag{1.12}$$

and similarly for vectors $\underline{\mathbf{a}} \in \mathbb{R}^{1\times N}$ and $\underline{\mathbf{b}} \in \mathbb{R}^{1\times N}$

$$\underline{\mathbf{a}} \odot \mathbf{b} = \{\underline{\mathbf{a}}\}_n \{\mathbf{b}\}_n \tag{1.13}$$

For complex valued matrices or vectors the same concept applies, except the real and imaginary components are multiplied with their respective values.

1.5 Overview

The remainder of this work is outlined as follows. In Chapter 2 a discussion the wireless channel phenomenology experiments used to model the UAS-to-ground channel are discussed. Additionally, the techniques used to derive the models from the empirical data are presented. Finally, a discussion of the final models and a characterization of their performance is presented.

In Chapter 3, the design concepts that comprise a joint sensing and communication system are discussed. Additionally, various two-node system topologies that can benefit from a joint sensing and communications design approach are outlined. Furthermore, the communications channel capacity and estimation rate performance metrics are presented. Finally, the corresponding performance bounds that arise from these metrics are discussed.

In Chapter 4, the joint multiple access receiver architecture is presented. A discussion of the radar and communications signal processing algorithms that compose the architecture is presented. Finally, variations of this architecture that arise due to different system topologies is discussed.

In Chapter 5, a discussion of the experimental implementation including waveforms, the WISCA SDR Network, and parameters is presented. Finally, performance bounds are generated experimentally using the system and discussed. In Chapter 6, a summary of this work as well as a discussion of future work is presented.

Chapter 2

THE UNMANNED AERIAL SYSTEM-TO-GROUND WIRELESS CHANNEL

In this chapter, a discussion of the methods used to study the phenomenology of the UAS-to-ground channel is presented. Generally UAS-to-ground channel phenomenology experiments consist of a large human piloted airplane communicating with a distant ground station. The experiments reported here focus primarily on characterizing the channel phenomenology using commercially available radio frequency (RF) components and small UAS (less than 20 kg) flying at altitudes of less than 130 meters. Furthermore, the experiments were conducted in mountainous desert and residential terrains. Finally, a discussion of the techniques used to construct channel models from the collected data is presented.

2.1 Wireless Channel Phenomenology Experiments

2.1.1 Terrain Descriptions

The experiments were conducted in two different terrains in the Phoenix, AZ metropolitan area. The first location was a neighborhood located in Chandler, AZ. The terrain is flat with homes situated between and around the receiver ground station and the flight path of the UAS. The receiver ground station was set up in a driveway of a home in the line of sight of the flight path of the UAS, as shown in Figure 2.1 (c). The UAS was flown in a park directly in front of the receiver ground station. The distance from the receiver to the farthest point of the UAS flight path was approximately 165 meters.

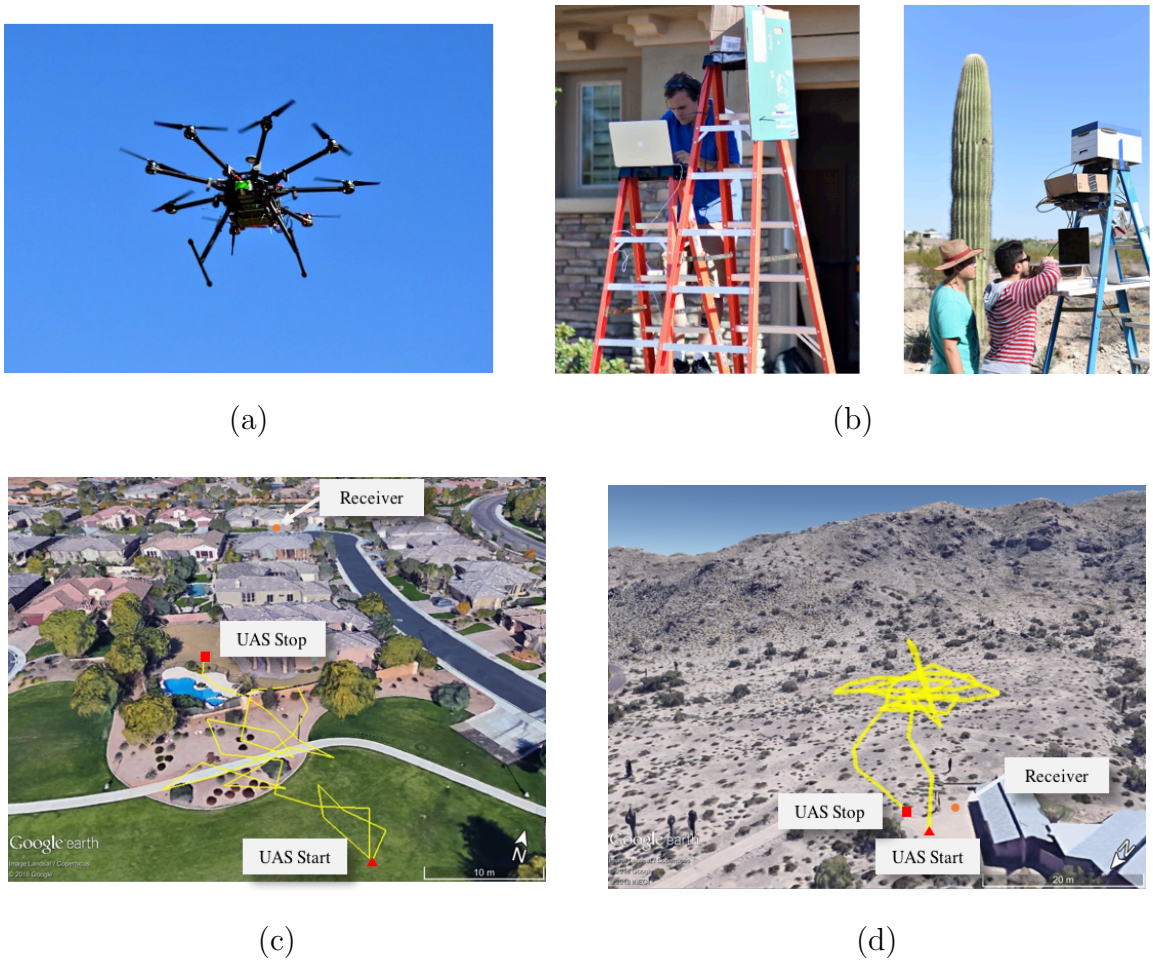

Figure 2.1: (a) DJI Spreading Wings 1000+ octocoper was used as the UAS transmitter beacon and the base stations consisted of a USRP B-210 mounted on top of a 2 meter tall ladder. (c)-(d) Images of the different experiment flight paths (minus elevation profiles), terrain, and location of base stations are shown. The flight paths were captured by GPS measurements from an Apple iPhone 5S that was part of the UAS payload.

The second location was near South Mountain Park located in Phoenix, AZ. The terrain was flat with minimal ground level scatterers. The location is in close proximity to parts of the South Mountain range, which acted as the primary scatterer. Similar to the residential experiment, the base station was set up in the line of sight the UAS at a distance of approximately 400 meters from the mountain. The location

of the base station as well as UAS is shown in Figure 2.1 (d). For each scenario, approximately 75 seconds worth of data was collected for analysis.

2.1.2 Measurement Instrumentation

For the experiments, a DJI Spreading Wings 1000+ octocopter was used as the UAS transmitter beacon. The UAS payload consisted of an Intel NUC (model D34010WYK), Ettus Research Universal Software Radio Peripheral (USRP) B-210 SDR transceiver, an iPhone 5S, and two lithium polymer batteries. The transceiver was mounted to the bottom of the UAS, such that the vertical antenna was facing the ground. The iPhone 5S was used to record the GPS position of the UAS.

The receiver ground station consisted of a USRP B-210 SDR transceiver and a 2014 MacBook Pro. In both experiments, the transceivers were perched atop of a 3 meter tall ladder. The MacBook Pro and Intel NUC controlled the radios, as well as stored transmit and receive data. Each transceiver was equipped with an oven-controlled crystal oscillator (OCXO) as the primary clock reference, and a vertically polarized (2.4 - 2.8 GHz and 4.9 - 5.9 GHz) dual-band omni-directional 3 dBi antenna.

The transmitter and receiver were both tuned to 5.8 GHz with a complex sample rate of $f_s = 30$ MHz. Images of both the UAS transmitter beacon and receiver ground stations are shown in Figure 2.1 (a) and (b). Further, a summary of the USRP B-210 RF specifications is presented in Table 2.1 (a).

2.1.3 Channel Sounding Waveform

A quadrature phase-shift keying (QPSK) modulated pseudorandom (PN) binary sequence was employed for the channel sounding waveform. The channel sounding waveform was generated in three stages. First, $2^{21} - 1$ PN binary bits were generated using a linear feedback shift register over Galois field [47]. Next, the binary sequence

Table 2.1: (a) USRP B-210 RF Specifications and (b) Experimental Parameters

RF Coverage	70 MHz-6 GHz
SSB/LO Suppression	-35/50 dBc
Power Output	>10 dBm
IIP3 (@typ NF)	-20 dBm
Receive Noise figure	<8 dB

(a)

PN Sequence Length	1.6×10^6
Amplifier Gain	89 dB
Complex Sample Rate	30 MHz
Complex Symbol Rate	20 MHz
Carrier Frequency	5.8 GHz

(b)

was modulated using quadrature phase-shift keying (QPSK). A re-sampler was used to upsample the QPSK sequence to 1.5 samples per symbol resulting in a 20 MHz complex symbol rate. Finally, a root raised cosine (RRC) pulse shaping filter was applied to the modulated waveform. The final waveform had a fractional bandwidth of $B_{\text{rms}}/f_{\text{c}} \approx 0.001$, where B_{rms} denotes the root-mean square bandwidth [48]. The RMS duration [48] of the waveform was $T_{\text{rms}} \approx 30.27$ ms. The spectrum of the channel sounding waveform is also shown in Figure 2.2. The waveform parameters are shown in Table 2.1 (b).

2.1.4 UAS Flight Path

The UAS was flown at approximately 120 m above ground level to stay in accordance with Federal Aviation Agency (FAA) restrictions — this is also the maximum allowed altitude within the flight control software. Other than takeoff and during certain maneuvers, the UAS remained at this height for the entire duration of the experiments. The UAS was flown in a back-and-forth pattern with occasional circular paths for both experiments. The distance from the receiver to the farthest point of the octocopter flight path was approximately 175 meters and 180 meters in the residential and desert experiments, respectively. Images of the environments along with

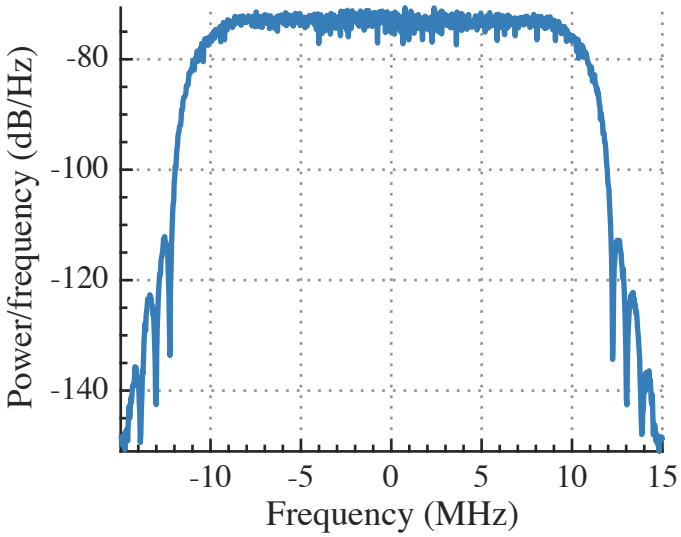

Figure 2.2: The spectrum of the channel sounding waveform used throughout both experiments. To generate the channel sounding waveform a PN sequence was generated using a GLFSR source and then encoded using QPSK modulation. The modulated waveform was then resampled to 1.5 samples per symbol and a RRC pulse shaping filter was applied to generate the final waveform.

the flight paths overlaid from the recorded iPhone 5S GPS data are shown in Figure 2.1 (c) and (d). We note here that the recorded GPS data during the experiments was relatively sparse due to drop outs in the GPS signals.

2.1.5 UAS Micro-Doppler Measurements

Before flying the octocopter, a single-input single-output (SISO) tone test was performed to build a micro-Doppler profile. The experiment was conducted in a laboratory environment using an Ettus USRP B210 and GNURadio Software. Transmit and receive patch antennas were placed approximately 15^o apart and directed towards the UAS. The experimental setup is shown in Figure 2.3.

A series of 100 kHz tones are transmitted and received at a 5.8 GHz carrier frequency. Two measurement sets were collected: transmission and reception while the motors were off, then transmission and reception with the motors on with the blades spinning. The spectral densities for each data set were estimated, compared,

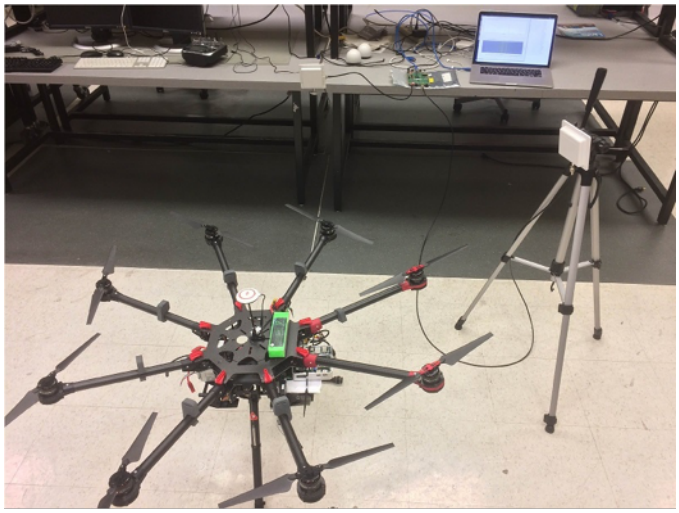

Figure 2.3: Electromagnetic micro-Doppler measurement experimental setup. A 100 kHz tone is transmitted at 5.8GHz with a sampling rate of 1MHz. Two 5.8GHz 11dBi flat patch antennas are used. Antenna height: 1.3m. Distance to drone: 1m. Angular separation: 15 degrees.

and whitened to produce an estimate of the micro-Doppler profile. A comparison of the transmit and receive spectral densities along with the whitened electromagnetic micro-Doppler estimate is shown in Figure 2.4.

The micro-Doppler profile shown in Figure 2.4 (a) consists of a set of tones centered around the transmission tone. These tones occur periodically with a period of about 50 Hz. Micro-Doppler spread around the transmission tone caused by the spinning blades is also visible. A "noise" subspace is constructed from the data with the blades off. The data with the blades on is then projected onto the subspace orthogonal to this noise subspace. The resulting whitened power spectral density is shown in Figure 2.4 (b). The periodic tones become more clearly identifiable. These tones are the result of rotor blade modulation on the impinging waveform while the peaks are the resulting harmonics of this effect. The micro-Doppler effect is also observed later in the Doppler power spectrum computed from the UAS air-to-ground channel measurements.

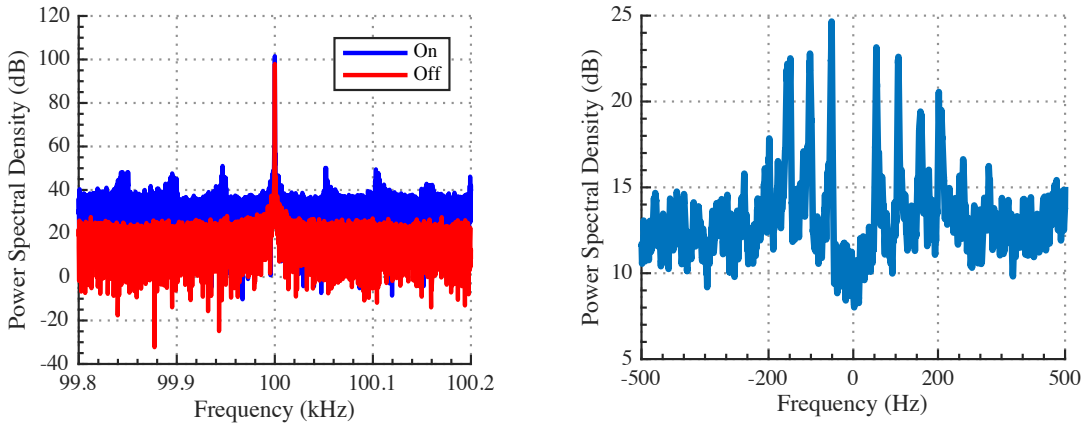

(a) (b)

Figure 2.4: Comparison of received power spectral densities when the blades are on and off. The received signal clearly exhibits micro-Doppler spread around the tone as a result of the spinning blades. Generated using 30s of data.

2.2 UAS-to-Ground Wireless Channel Characterization

A complete characterization of the wireless channel is described by three components: path loss, shadowing, and multipath [49]. The first two components describe large-scale fading, while the third component describes small-scale fading. Due to the line-of-sight nature of the experiments, large-scale fading is modeled using a simplified free-space path loss model with normal distributed shadow fading [49].

For small-scale fading a narrowband time and frequency dispersive Wide-Sense Stationary Uncorrelated Scattering (WSSUS) [50] channel model is considered. This model is appropriate to characterize the channel due to the small fractional bandwidth of the waveform, the relatively slow velocity of the UAS, and the fixed base station. The WSSUS assumption is verified by computing stationarity regions based on empirical correlations of successive power delay profiles [51] in Section 2.3.

2.2.1 Large-Scale Fading

A simplified path loss model for the attenuation observed by the receiver is

$$P_r = \beta\, d^{-2} \tag{2.1}$$

where β denotes the unit less constant that represents losses due to environment and d is distance between the transmitter and receiver. We express Equation (2.1) in dB and include the normal distributed shadowing variable to obtain the final model

$$P_r\,\mathrm{dB} = \beta\,\mathrm{dB} - 20\,\log_{10}(d) + \psi\,\mathrm{dB}, \tag{2.2}$$

where $\psi \sim \mathcal{N}(0,1)$. Other minor factors that influence path loss including the orientation of the antenna on the UAS, and the type of the UAS, are considered negligible.

For the model, the parameter β is estimated from the UAS GPS longitude and latitude readings during flight, as well as the estimated per sample receive power. The received power is estimated

$$P_r \approx \underline{\mathbf{z}}\,\mathbf{P_s}\,\underline{\mathbf{z}}^{\dagger} \tag{2.3}$$

$$\mathbf{P_s} = \mathbf{S}^{\dagger}\,(\mathbf{S}\,\mathbf{S}^{\dagger})^{-1}\,\mathbf{S} \tag{2.4}$$

$$\mathbf{S} = \begin{bmatrix} \mathbf{s}(\delta_0) & \mathbf{s}(\delta_1) & \dots & \mathbf{s}(\delta_{\text{L-1}}) \end{bmatrix}^{T}, \tag{2.5}$$

where ^{T} denotes the non-Hermitian transpose, $\mathbf{P_s}$ denotes the orthogonal projection of matrix $\mathbf{S}$, and $\underline{\mathbf{z}} \in \mathbb{C}^{1\times N}$ denotes N samples of the received waveform. The rows of matrix $\mathbf{S} \in \mathbb{C}^{L\times N}$ consist of the transmitted waveform at delays $\{\delta_0, \delta_1, \dots, \delta_{L-1}\}$, where L denotes the number of delays.

The model parameter β was estimated using polynomial regression and calculated as $\beta = 31$ dB for the desert environment and $\beta = 39$ dB for the residential environment. Plots of the measured receive power and the model versus link distance for both environments are shown in Figure 2.5. We note here that the GPS data used

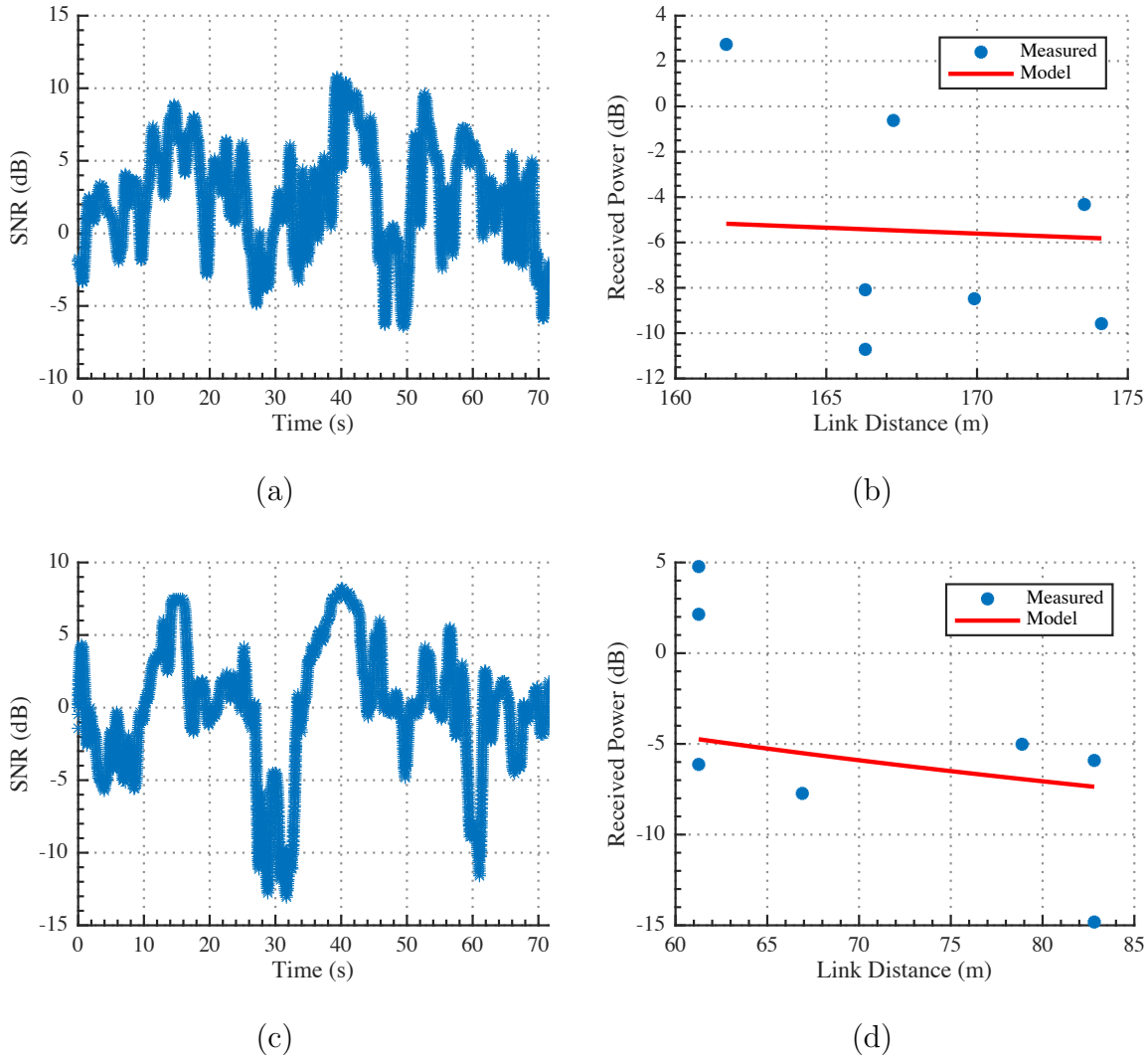

Figure 2.5: Plots of the estimated SNR over time and path loss fits compared to the empirical data for the (a) – (b) residential and (c) – (d) desert environments. Deep fades in SNR are visible at multiple time instances throughout the data in both environments. Received power decreases as a linear function in dB.

to estimate the model parameters was limited due to GPS dropouts that occurred during the time of the flights. The model does not provide a good representation of the empirical data. We suspect this is due to amplitude calibration errors or strong ground bounce, but further investigation is needed. For reference, the estimated SNR versus time is shown in Figure 2.5.

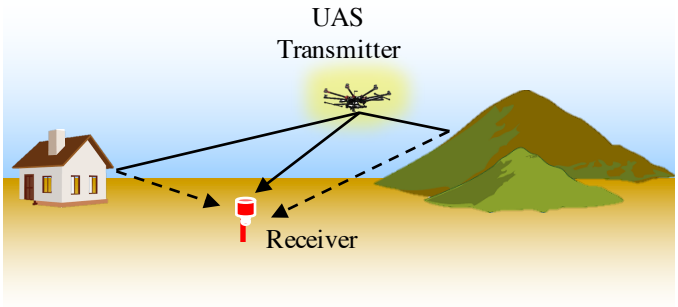

Figure 2.6: Illustration of multipath environment for a UAS-to-ground communications scenario. Multipath fading is induced by objects in the vicinity of the UAS transmitter and ground based receiver. Several of these objects include the ground, mountains, homes, and brush to name a few.

2.2.2 Small-Scale Fading

For a narrowband environment, like the one considered in this work, the input/output relationship of the channel is represented by [49]

$$y(t) = \int_{-\infty}^{\infty} h(\tau, t)\, x(t-\tau)\, d\tau, \tag{2.6}$$

where $h(\tau, t$ denotes the impulse response of the channel at time t and delay τ. In practice, reflectors and scatterers in the environment induce *multipath fading*, which causes multiple versions of the transmitted waveform to arrive at the receiver. Each version of the transmitted waveform is distorted in amplitude, phase and angle of arrival. Furthermore, mobility of the transmitter or receiver (or both) introduces a frequency or *Doppler shift* component to the signal.

Considering all of these effects, the WSSUS narrowband multipath environment is modeled as a summation of P discrete resolvable paths [52, 53]

$$h(t, \tau) = \sum_{p=0}^{P-1} z_p(t)\, \alpha_p(t)\, \exp\{j\, \nu_p(t)\}\, \delta(t - \tau_p(t)) \tag{2.7}$$

at complex baseband. The parameters $\alpha_p(t)$, $\nu_p(t)$, and $\tau_p(t)$ are the time-varying complex amplitude, Doppler frequency, and propagation delay of the $p-$th multipath

component, respectively. The function $z_p(t)$ represents the multipath persistence process [53]. The multipath persistence process models the on/off behavior of the multipath components that often occurs in a highly mobile environment with a large number of scatterers. This is often implemented using a Markov chain. Given the line-of-sight (LoS) nature of the channel, the multipath components of the model will always be on. Thus, the persistence process is not modeled.

The equivalent discrete-time baseband model is given by [54]

$$y[n] = \sum_{\ell} h_\ell[n]\, x[n-\ell], \tag{2.8}$$

$$h_\ell[n] = \sum_{p=0}^{P-1} \alpha_p[n]\, \exp\{-j\, 2\,\pi\nu_p\, n\}\, \mathrm{sinc}(\ell - \tau_p[n]\, f_s), \tag{2.9}$$

where ℓ denotes the complex channel filter tap index at time instant n and f_s denotes the complex sampling frequency. Under the WSSUS assumption, the model parameters are assumed to be constant within a small estimation time window and vary slowly beyond this time window. Thus, the time dependence of Equation (2.9) is removed and the discrete time channel model is given by

$$h[\ell] = \sum_{p=0}^{P-1} \alpha_p\, \exp\{j\, \nu_p\}\, \mathrm{sinc}(\ell - \tau_p\, f_s). \tag{2.10}$$

In this work, the wireless channel is characterized by the parameter set $\theta = \{\alpha_p,\, \nu_p,\, \tau_p,\, P\}$. The channel model in Equation (2.10) is referred to as *time-frequency* selective or doubly dispersive [48] since the channel induces fading over both time and frequency.

2.2.3 Extracting Model Parameters from Data

A statistical model of the channel can be derived from empirical data by evaluating the cross ambiguity function (CAF) or *scattering function* [48, 55] over multiple time instances. The CAF combines information about Doppler spread and the path

delays and is computed by correlating known frequency shifted versions of the sampled transmit signal, $\underline{\mathbf{x}} \in \mathbb{C}^{1\times N}$, with the sampled noisy receive signal, $\underline{\mathbf{y}} \in \mathbb{C}^{1\times N}$. Mathematically, the discrete-time CAF matrix for a single time instance t is expressed as

$$\{\mathbf{A}_t\}_{m,k} = \frac{1}{N}\sum_{n=0}^{N-1} \{\underline{\mathbf{x}}\}^*_{n+m}\ \{\underline{\mathbf{y}}\}_n \exp\left\{\frac{-j\,2\pi\,k\,n}{N}\right\}, \tag{2.11}$$

where $\mathbf{A}_t \in \mathbb{C}^{2\,M\times K}$ for $t = 0, 1\ldots, T_{\text{tot}}$ where T_{tot} denotes the total number of time instances considered, N is the time support in samples, $m = -M, -M+1, \ldots, M-1, M$ is the time delay index, and k/N is the digital frequency or fraction of the sampling frequency. Plots of magnitude surface of the CAF for one time instance in both environments are shown in Figure 2.7 (a) and (b). The peak value of the magnitude provides an estimate of the delay and Doppler of the channel. A plot of the Doppler frequency estimate over time for both environments is shown in Figure 2.7 (c) and (d).

The channel impulse response for a single time instance t is estimated from the CAF by summing over the entire range of CAF frequencies

$$\mathbf{h}_t = \sum_{k=-K}^{K} \{\mathbf{A}_t\}_{m,k} \tag{2.12}$$

where $\|\cdot\|$ denotes the L_2 norm. The estimated energy of each multipath component is

$$\mathbf{p}_t = \|\mathbf{h}_t\|^2, \tag{2.13}$$

and is known as the *instantaneous power delay profile* or *multipath intensity profile*. The root mean square (RMS) delay spread provides a measure of the time delay

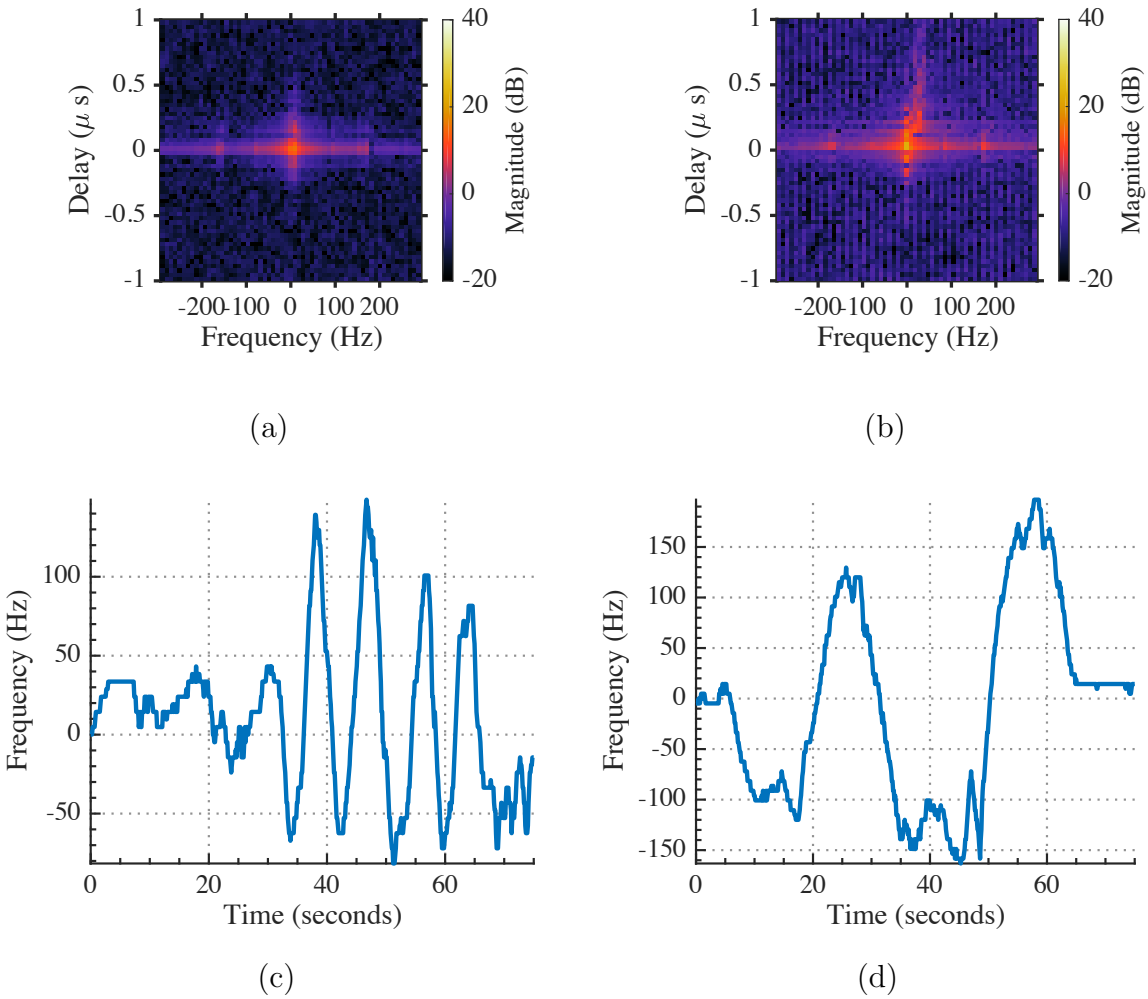

Figure 2.7: (a)-(b) Pseudocolor images of the magnitude of the CAF provide us with a visualization into the Doppler and delay spread of the propagation environment. (c)-(d) Plots of the time evolution of the maximum Doppler frequency offset provide us with a rough estimate of the radial velocity relative to the receiver.

extent of the channel and is defined by

$$\sigma_\tau = \left(\frac{1}{P_c} \sum_{m=0}^{M} \{\tilde{\mathbf{p}}_t\}_m \, (m\,T_s)^2 - \tau^2 \right)^{1/2} \tag{2.14}$$

$$P_{\mathrm{c}} = \sum_{m=0}^{M} \{\tilde{\mathbf{p}}_t\}_m \tag{2.15}$$

$$\tau = \frac{T_s}{P_{\mathrm{c}}} \sum_{m=0}^{M} \{\tilde{\mathbf{p}}_t\}_m \, m \tag{2.16}$$

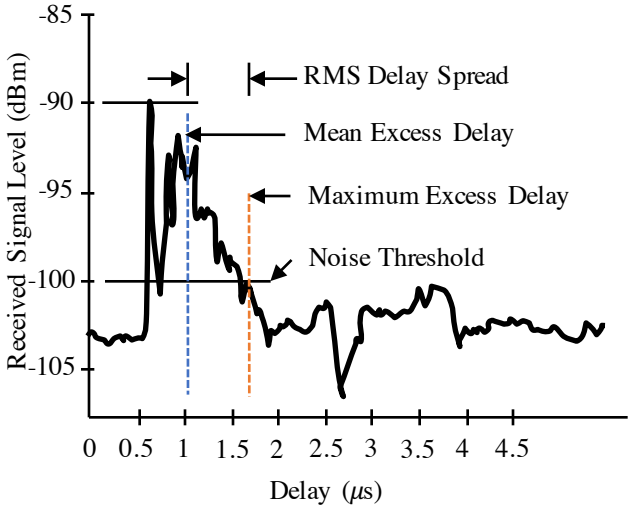

Figure 2.8: The power delay profile provides the distribution of the signal power received from the multipath channel as a function of propagation delay. Two characteristics include the mean and maximum excess delay. Another widely used characteristic is the root mean square delay spread, which is the value of multipath reflections, weighted proportional to the energy in the reflected waves.

where $\tilde{\mathbf{p}}_t$ denotes a threshold version of the power delay profile vector at time instance t. This vector is formed by discarding elements that fall below 30 dB of the maximum value. In Equation (2.16) the variables T_s, P_c, and τ denote the sampling period, *total channel power*, and *mean delay*, respectively. An illustration of the power delay profile and associated attributes is shown in Figure 2.8.

Similar to the power delay profile, the *Doppler power spectrum* provides the distribution of the signal power received from the multipath channel in the frequency domain [48]. The Doppler power spectrum is derived by summing over the entire range of CAF delay values

$$\mathbf{s}_t = \sum_{m=-M}^{M} \|\{\mathbf{A}_t\}_{m,k}\|. \tag{2.17}$$

It should be noted that estimating the Doppler spectrum via Equation (2.17) does not completely isolate the Doppler spectrum from low frequency phase noise introduced

by the local oscillator. However, most local oscillators have very low phase noise profiles and thus, it assumed that Doppler is the dominant behavior.

2.3 UAS-to-Ground Wireless Channel Modeling

As mentioned in Section 2.2.2, the channel model considered in this work is *doubly dispersive*. That is, the channel exhibits dispersion in both the time and frequency domains. The channel is assumed to be WSSUS, thus the time and frequency dispersion processes are modeled independently. The WSSUS assumption is verified in this section using local regions of stationarity, but this assumption has been shown to hold in similar outdoor non-vehicle-to-vehicle channel environments [56]. To simulate both processes filtered Gaussian noise techniques are employed [57]. These techniques consider a type of model where the complex multipath amplitudes, α_p, are generated from a random process with a Rician or Rayleigh distribution, filtered by a Doppler filter, and then scaled to a specified average power.

2.3.1 Path Selection

To select the paths of the model, P, delay values, τ_p, and average powers, $\|\alpha_p\|^2$, power delay profiles were computed throughout the entire data using a sliding window technique. A window size of $N = 30000$ samples, or approximately 1 millisecond, was used. The window size was chosen such that it was small enough the Doppler effect would not be observed. For both environments, an ensemble of 85932 power delay profiles were extracted.

To reduce fluctuations due to time-selective fading, groups of thresholded power delay profiles were averaged together to obtain smoothed versions of the power delay

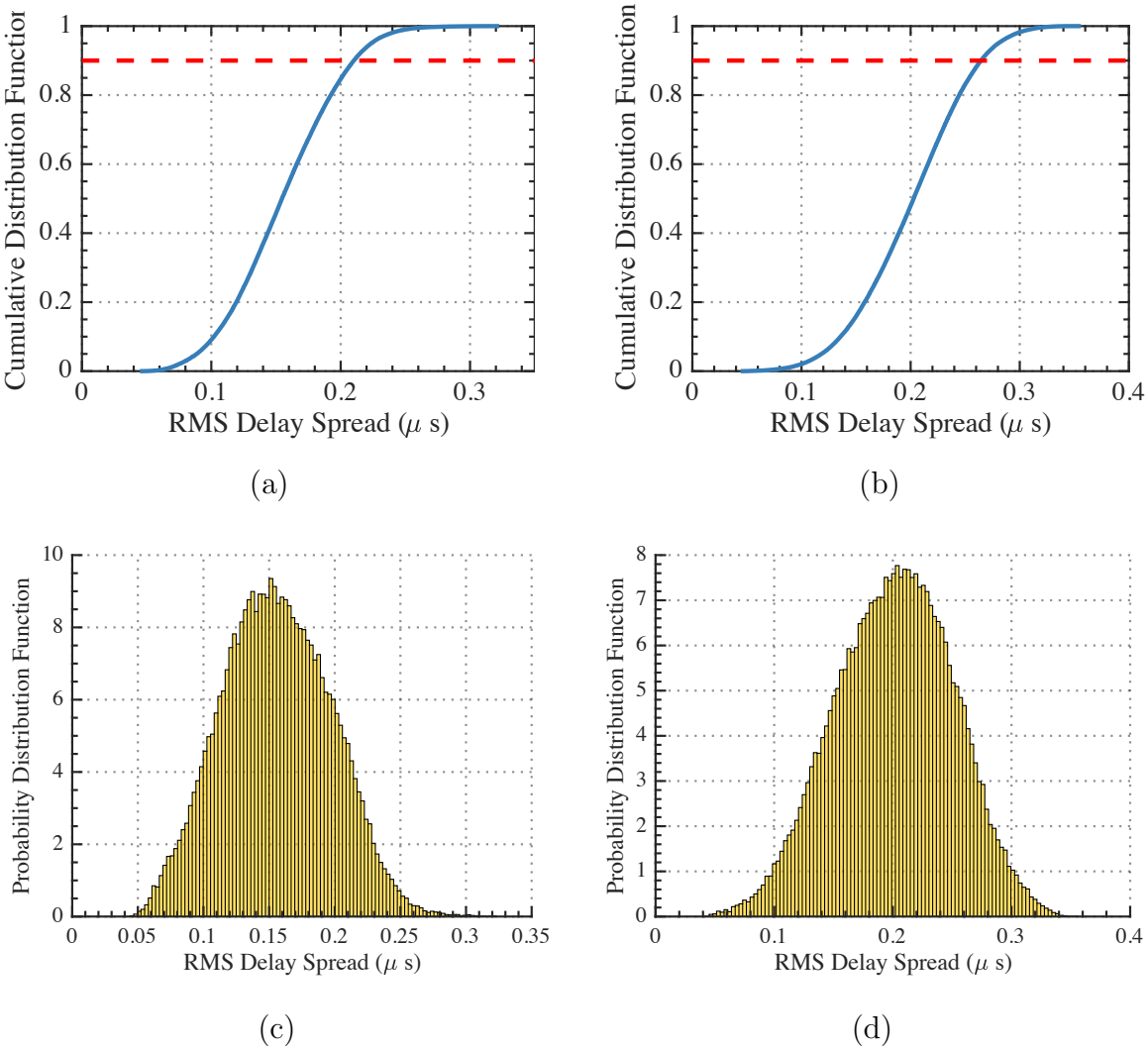

Figure 2.9: The cumulative and probability distribution functions for the RMS delay spreads provide insight to the range of spreads that are induced by the environment. Longer RMS delay spreads are observed in the desert environment ((b) and (d)) relative to the residential environment ((a) and (c))

profiles

$$\overline{\mathbf{p}}_t = \frac{1}{\Delta t} \sum_{t=0}^{t+\Delta t-1} \tilde{\mathbf{p}}_t, \tag{2.18}$$

where $\Delta t = 100$ denotes the the sliding average window size or the number of power delay profiles to be averaged.

To verify the WSSUS assumption, a temporal power delay profile correlation coefficient metric [51] was computed between consecutive average power delay profiles:

$$c[t] = \frac{\overline{\mathbf{p}}_t^{\dagger}\,\overline{\mathbf{p}}_{t+1}}{\max\left\{\|\overline{\mathbf{p}}_t\|^2, \|\overline{\mathbf{p}}_{t+1}\|^2\right\}}. \tag{2.19}$$

In both environments, all the correlation coefficients were greater than 0.9 which indicated that each power delay profile was similar to each other. Thus confirming the WSSUS assumption throughout the entire data set. The RMS delay spread was evaluated using the average power delay profiles to determine the appropriate number of paths P.

The number of paths, P, for the model is chosen to be equal to the RMS delay spread that accounts for 90% of the distribution shown in Figure 2.7 (c) and (d). Let $\overline{\sigma}_\tau$ denote the RMS delay spread value that meets the aforementioned criteria, the number of paths is computed as

$$P = \left\lceil \frac{\overline{\sigma}_\tau}{T_s} \right\rceil, \tag{2.20}$$

where $\lceil \cdot \rceil$ represents the ceil operator. The threshold values occur at approximately $0.21\,\mu$s (6 multipath components) and $0.26\,\mu$s (8 multipath components) for the residential and desert environment, respectively.

2.3.2 Average Path Gains

The complex amplitude process, α_p, is influenced by three components: amplitude distribution, power delay profile, and the Doppler power spectrum. In the following section, the methods of modeling each component is presented. A summary of the overall channel model parameters for each environment are presented in Table 2.2 and Table 2.3.

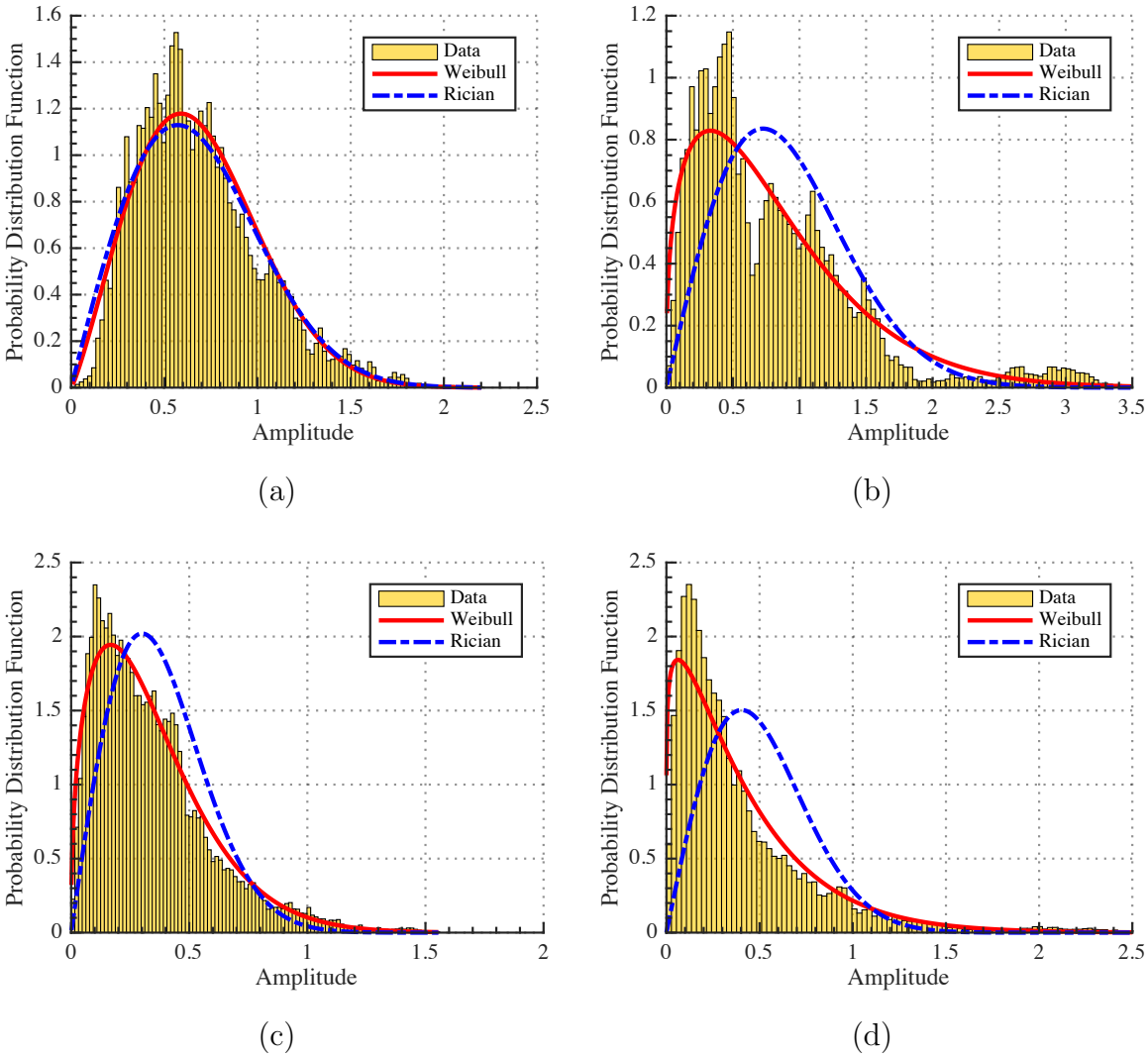

Figure 2.10: Comparison of Rician and Weibull probability distribution function fitted to empirical data collected in the residential and desert environments. For brevity, only the first and second delay amplitude distributions are shown. The distributions in (a) and (c) are the first and second delay amplitudes for the residential environment. The Weibull distribution provides the best fit among both delay amplitudes, although the Rician distribution fit is also in good agreement with the first delay amplitude data. The distributions in (b) and (d) are the first and second delay amplitude data for the desert environment. Here, the Weibull distribution provides the best fit among both delay amplitude data.

Amplitude Distributions

In the channel sounding experiments line of sight (LoS) was maintained between the transmitter and the receiver. In this case the multipath amplitudes are often described

by a complex exponential (the LoS component) and a narrowband Gaussian process (the diffuse component), which follows the *Rician* distribution.

Maximum likelihood estimation was employed to fit a Rician distribution to the empirical data. For reference, histograms of the first and second delay amplitudes of the empirical data for both scenarios along with Rician distribution fit are shown in Figure 2.10. The Rician distribution provides a decent approximation of the empirical data in each case, but not the best.

The Weibull distribution [58] however, provides the best fit for the largest number of delay amplitudes. The amplitude of the complex univariate Weibull distribution is [59]

$$p_H(h; a, b) = a\, b\, h^{b-1} \exp\left\{-a\, h^b\right\} \tag{2.21a}$$

$$a = \left[\Gamma\left(\frac{2}{b} + 1\right)\right]^{\frac{1}{2}} \tag{2.21b}$$

$$\Gamma(n) = (n-1)\,! \tag{2.21c}$$

where $h = \|\{\mathbf{h}_t\}_m\|$ is the amplitude of the m^{th} channel delay and a single realization of the Weibull random variable H. The Weibull distribution offers substantial flexibility because it is governed by two parameters a and b, where $a > 0$ and $b > 0$ controls the scaling and shaping. The Weibull distribution coincides with the exponential distribution when $b = 1$ and the Rayleigh distribution when $b = 2$.

An illustration of the Weibull probability distribution fit to the empirical data for each environment is shown in Figure 2.10. In each case, the fitted distributions are in good agreement with the empirical data. A summary of the Weibull shaping parameters for each path for the residential and desert environment is provided in Table 2.2 and Table 2.3.

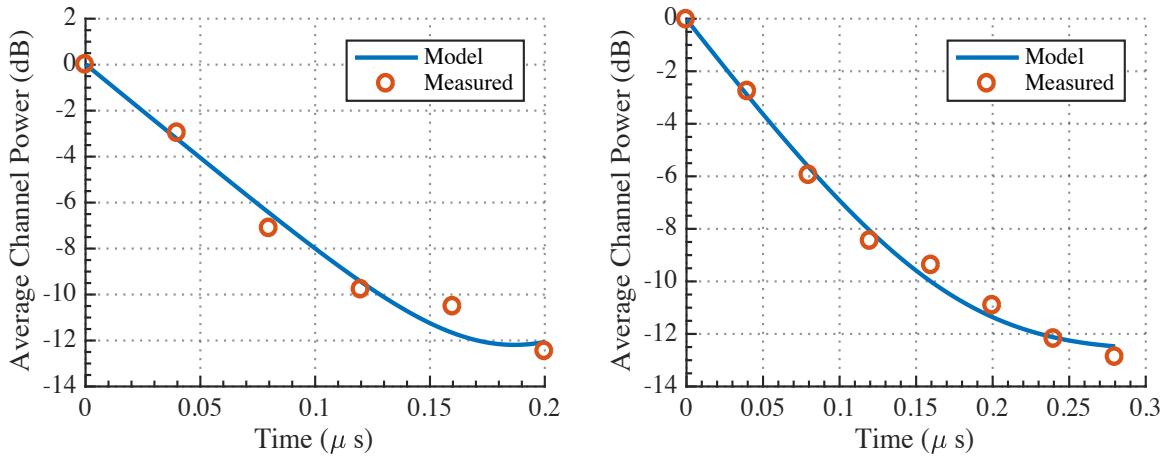

(a) (b)

Figure 2.11: The average channel power is a good approximation of a single representative tapped delay line model for the environments. Plots for the average channel power and the associated exponential fits for (a) the residential and (b) desert environments.

Power Delay Profile Model

The power delay profile model was computed by evaluating the average across the smoothed power delay profile estimates

$$\mathbf{p}_{\text{final}} = \frac{1}{T}\sum_{t=0}^{T-1}\overline{\mathbf{p}}_t, \tag{2.22}$$

where T denotes the total number of average power delay profiles. The average channel power curves for both environments are shown in Figure 2.11. The average channel power curves follow the general exponential decay function of the form

$$\mathcal{E}[p] = \sum_{i=1}^{I} a_i \, \exp(-b_i \, p). \tag{2.23}$$

For the model, a value of $I = 2$ exponential functions produced the best fit across all multipath components. To determine the parameters a and b for both environments *least squares* regression was employed. The resulting fits for the models along side the measured data are shown in Figure 2.11.

Table 2.2: Summary of Model Parameters Residential Environment

Number of Paths	6
Exponential Decay Parameters	$a_1 = 1.03 \quad b_1 = 18.86$
	$a_2 = 0.001 \quad b_2 = -18.14$
Weibull Shaping Factors	Path 1 a=0.78 b=2.2
	Path 2 a=0.38 b=1.44
	Path 3 a=0.13 b=1.98
	Path 4 a=0.07 b=1.56
	Path 5 a=0.06 b=1.8
	Path 6 a=0.04 b=1.9
Spectral Shaping Parameters	$a_1 = 0.8 \quad b_1 = -4.74 \quad c_1 = 7.45$
	$a_2 = 0.16 \quad b_2 = -4.01 \quad c_2 = 36$
	$a_3 = 0.03 \quad b_3 = -2.49 \quad c_3 = 415$
Path Loss Parameters	$\beta = 39$ dB $\quad \gamma = 2$

Doppler Power Spectrum

To determine the overall Doppler power spectrum for each delay value the line-of-sight components of the spectra were aligned and averaged across the 650 segments. A similar approach is used in Reference [60] to derive a Doppler spectrum model for the vehicle-to-vehicle channel. The overall Doppler spectrum for both environments is shown in Figure 2.12 (a). For comparison, the Doppler spectrum of the transmitted sequence is also shown.

Several common Doppler power spectra models for fading processes are reviewed in [61], along with their theoretical and/or empirical motivation. A typical model that is used in air to ground channel modeling is the Gaussian Doppler spectrum [62]. The observed spectrum exhibits Gaussian characteristics, thus a sum of three

Table 2.3: Summary of Model Parameters Desert Environment

Number of Paths	8
Exponential Decay Parameters	$a_1 = 0.96 \quad b_1 = 24.81$
	$a_2 = 0.03 \quad b_2 = -1.68$
Weibull Shaping Factors	Path 1 a=0.89 b=1.36
	Path 2 a=0.43 b=1.13
	Path 3 a=0.18 b=1.33
	Path 4 a=0.1 b=1.21
	Path 5 a=0.08 b=1.28
	Path 6 a=0.05 b=1.31
	Path 7 a=0.03 b=1.38
	Path 8 a=0.03 b=1.37
Spectral Shaping Parameters	Same as Residential
Path Loss Parameters	$\beta = 31$ dB $\quad \gamma = 2$

Gaussian functions of the form

$$S[k] = \sum_{i=1}^{3} a_i \exp\left\{ -\left(\frac{|k - b_i|}{c_i} \right)^2 \right\}, \tag{2.24}$$

are fit to the data. The variables a_i, f_i , and c_i denote the amplitude, Doppler shift, and dispersion of the i^{th} Gaussian function. By using multiple Gaussian functions a much better representation of the Doppler spectrum is obtained. In Figure 2.12, a plot of the measured Doppler spectrum and the corresponding model for both environments are shown.

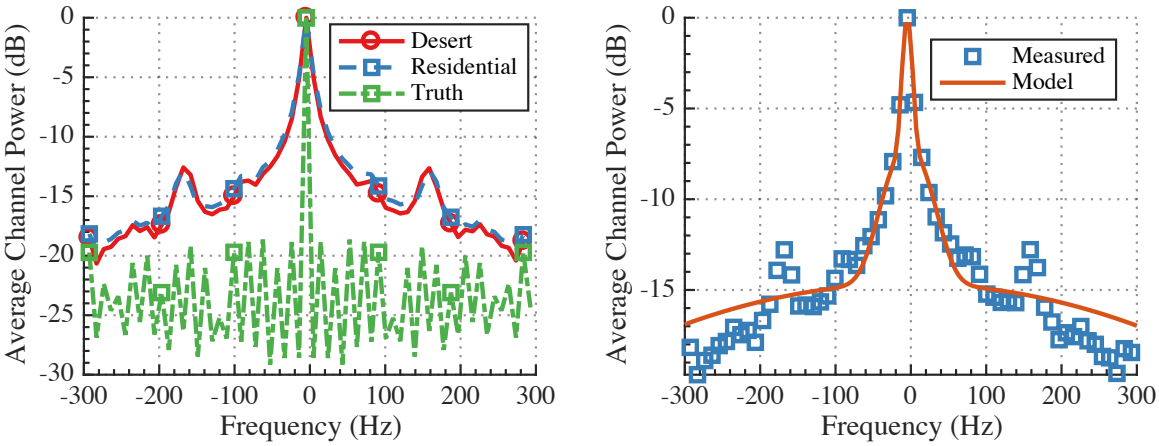

(a) (b)

Figure 2.12: (a) The average Doppler power spectrum provides an estimate of the spectral broadening that occurs as a result of the environments. Here, the measured average Doppler spectrums for both environments are compared to the truth sequence. (b) Doppler spectrum of the measured data along with Gaussian model fit using three Gaussian functions. The model approximates the overall shape and spread very well. However, the model doesn't quite capture some of the subtleties such as the peaks at ± 150 Hz caused by the motion of the octocopter blades.

2.3.3 Model Validation

To validate the accuracy of the proposed models a filtered Gaussian noise simulator was constructed using the parameters specified in Table 2.2 and Table 2.3. Given

$$y[n] = \sum_{\ell=L_1}^{L_2} h[\ell]\, x[n-\ell] \tag{2.25}$$

where $h[\ell]$ denotes the channel coefficients generated by

$$h[\ell] = \sum_{p=0}^{P-1} \alpha_p[\ell]\ \mathrm{sinc}\left(\ell - \tau_p\, f_s\right), \tag{2.26}$$

and $L_2 - L_1 + 1$ is the length of the channel filter where the channel power is effectively zero if ℓ is less than L_1 or greater than L_2.

Each path gain process α_p is generated in the following manner:

1. Generate zero mean, unit variance complex Gaussian noise coefficients $\underline{\mathbf{r}}_p \sim \mathcal{CN}(0,1)$;

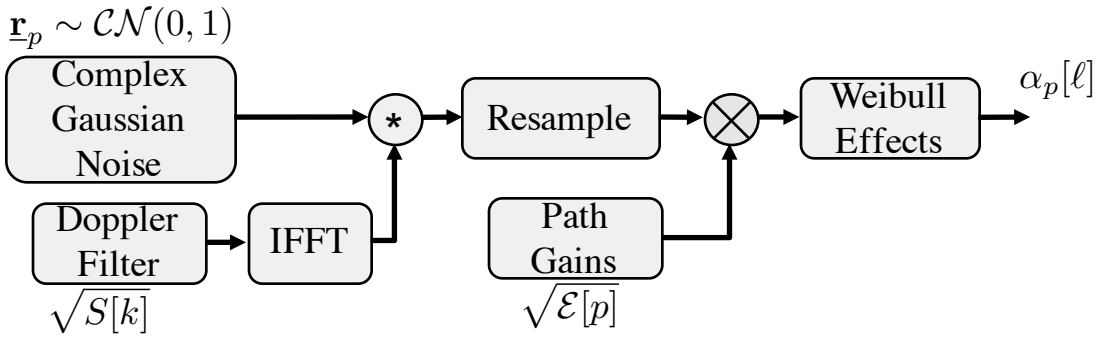

Figure 2.13: Illustration of the channel simulation process. A zero mean, unit variance complex Gaussian noise process is generated and then filtered with a corresponding Doppler filter in the frequency domain. The result of this process is then scaled by the average path gain coefficients in the time domain. The final path gain process is generated by adding in the Weibull effects according to Equation (2.27).

2. Filter $\underline{\mathbf{r}}_p$ with Doppler filter, $S[k]$, in frequency domain to obtain sequence. Doppler filter is constructed over the frequency range -200 Hz to 200 Hz;

3. Interpolate filtered complex Gaussian process to sample frequency consistent with that of the input signal.

4. Incorporate Weibull effects via method of norms [59, 63]

The Weibull effects are incorporated into the final path gain process in the following manner. Let $\underline{\mathbf{z}}_{\mathrm{CN}} \in \mathbb{C}^{1\times R}$ denote the vector of samples at the output of the re-sampler and $\underline{\mathbf{z}}_{\mathrm{WN}} \in \mathbb{C}^{1\times R}$ denote a vector of samples drawn from the Weibull distribution given in Equations (2.21a) to (2.21c). The final gain for path p is obtained via

$$\alpha_p[\ell] = \sqrt{\mathcal{E}[p]}\,\underline{\mathbf{z}}_{\mathrm{CN}}\,\frac{\|\underline{\mathbf{z}}_{\mathrm{WN}}\|}{\|\underline{\mathbf{z}}_{\mathrm{CN}}\|}. \tag{2.27}$$

where $\alpha_p[\ell]$ denotes the path gain process for the ℓ^{th} channel coefficient. The channel generation process is illustrated in Figure 2.13

Using this process, a total of 10,000 model-derived power delay profiles were generated and their corresponding RMS delay spread distributions were computed. The

quality of the model parameters were evaluated on the basis of how well the simulated RMS delay spreads and their distributions agree with the measured data. Similar approaches are used in References [64–66].

To quantify the model mismatch the Kullback-Leibler (KL) divergence [67] used to calculate the relative entropy between the measured and simulated RMS delay spread probability distribution functions. Let P_{m} and Q_{s} denote the respective probability distribution functions of the measured data and simulated model, the KL divergence is

$$D_{\mathrm{KL}}(P_{\mathrm{m}}||Q_{\mathrm{s}}) = \sum_{i=1}^{I} P_{\mathrm{m}}(i) \log_2 \left\{ \frac{P_{\mathrm{m}}(i)}{Q_{\mathrm{s}}(i)} \right\}, \tag{2.28}$$

where I represents the number points within the distribution range. If the probability distributions are identical $D_{\mathrm{KL}}(P_{\mathrm{m}}||Q_{\mathrm{s}}) = 0$, thus smaller divergence values indicate that the model is a good match of the underlying data.

For the KL divergence analysis, it is proposed that a KL divergence score of less than 0.06 represents the threshold that a the model accurately describes the underlying empirical data. To determine this value KL divergence scores were computed between two zero mean and unit variance Gaussian distributions. The cumulative distribution of 500 scores was analyzed and the score that encompassed the entire distribution was selected. The cumulative distribution of the KL divergence scores is shown in Figure 2.15.

In Figure 2.14 plots of the cumulative and probability distribution functions are shown for the measured and simulated RMS delay spreads in both environments. The models produce distributions that adequately characterize the measured distributions. Both models produce RMS delay spread distributions that match both the spread and intricacies of the distribution of the measured data. For verification, we quantify both fits using the KL divergence metric.

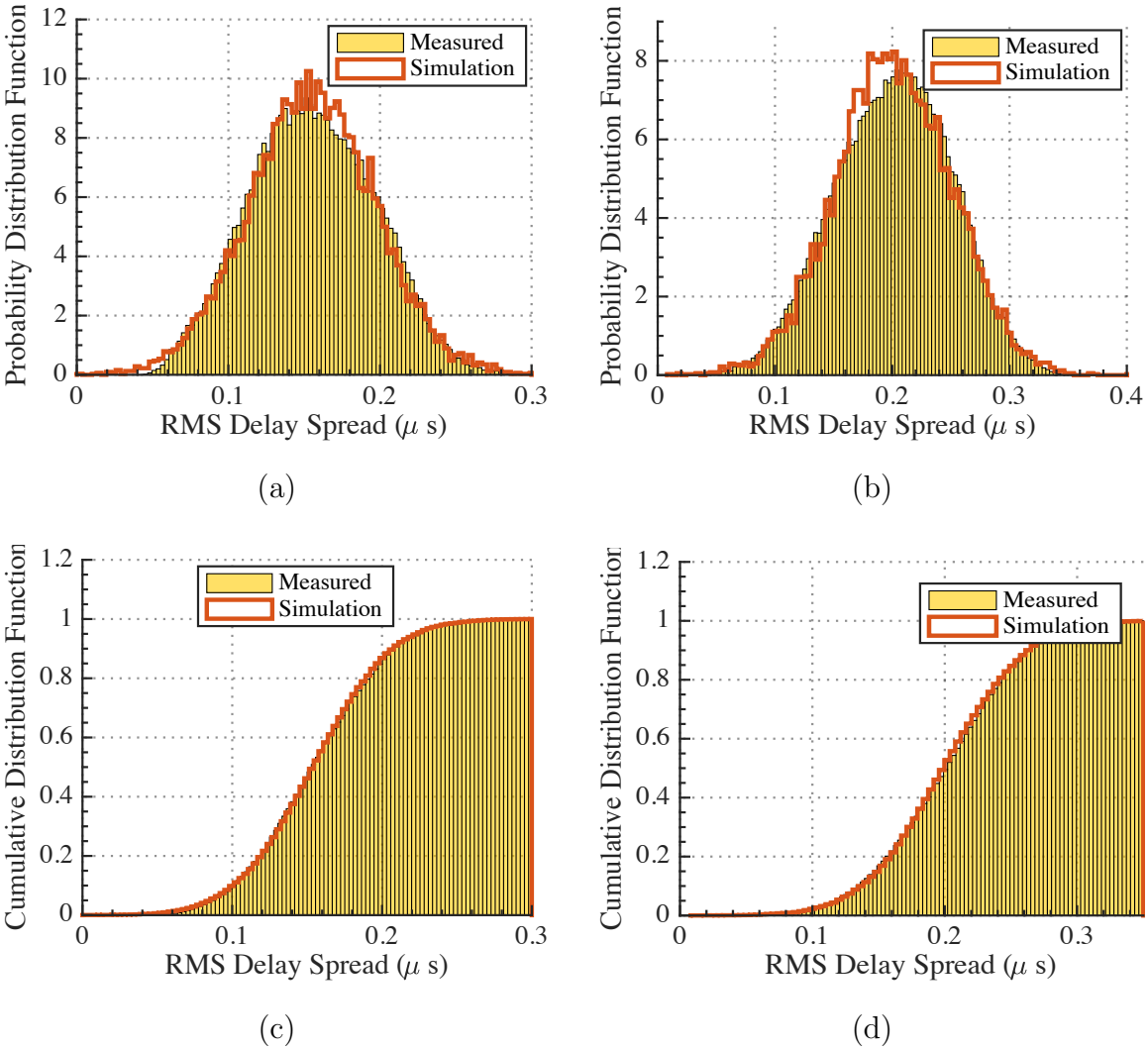

Figure 2.14: A comparison of the measured versus simulation probability and cumulative distribution functions (PDF and CDF) for the RMS delay spread. The distributions were estimated via a kernel density estimator. The RMS delay spread of the models capture the major characteristics of the distributions.

A summary of the corresponding KL divergence scores are presented in Table 2.4. Both models are fairly good matches to the measured data given their small KL divergence values. However, the desert model provides a better overall representation of the data than the residential model. The desert model better characterizes the subtleties of the measured data that are not captured by the residential model.

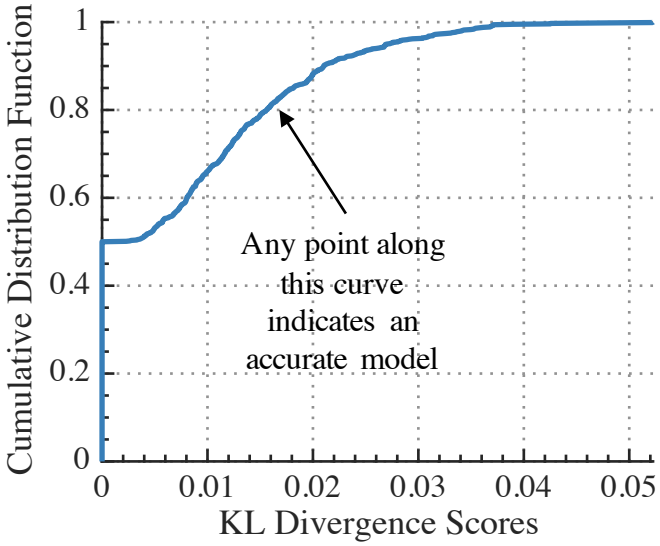

Figure 2.15: KL divergence scores between zero-mean unit-variance Gaussian distributions were compared to determine a score threshold score that constitutes an accurate model. A threshold value of 0.06 was selected because it encompassed the entire distribution.

Table 2.4: KL Divergence of RMS Delay Spread Distribution

Environment	Simulation
Residential	0.03
Desert	0.02

Chapter 3

JOINT SENSING AND COMMUNICATION SYSTEMS

A joint sensing and communication system can be defined as one or more transceiver nodes that perform various radar and communication functions simultaneously. By this definition, the number of system design concepts are limited. However, the variations of system topologies that exist are abundant. In this chapter, a description of the various system design concepts that arise from the joint sensing and communications problem are presented. Additionally, a representative subset of these system topologies is discussed. For simplicity, the discussion is limited to two-node topologies. Finally, the performance metrics and bounds that characterize the performance of a joint sensing and communications system is presented.

3.1 System Design Concepts

The system design concepts of the joint sensing and communications problem can be grouped broadly into four categories: isolation, coexistence, cooperation, and co-design [3]. Block diagram representations for each of these concepts are shown in Figure 3.1. Isolation is the concept where each node performs either a radar or communications function, but not both. During the design process no attempt is made to integrate radar or communication functions at each node [3]. The current solution is to regulate the operating frequencies that each communications and radar node operates. Realistically, perfect isolation is not achievable and each node is susceptible interference from each other.

The coexistence design concept is another legacy solution where both radar and communications nodes mitigate interference from each other. However, no commu-

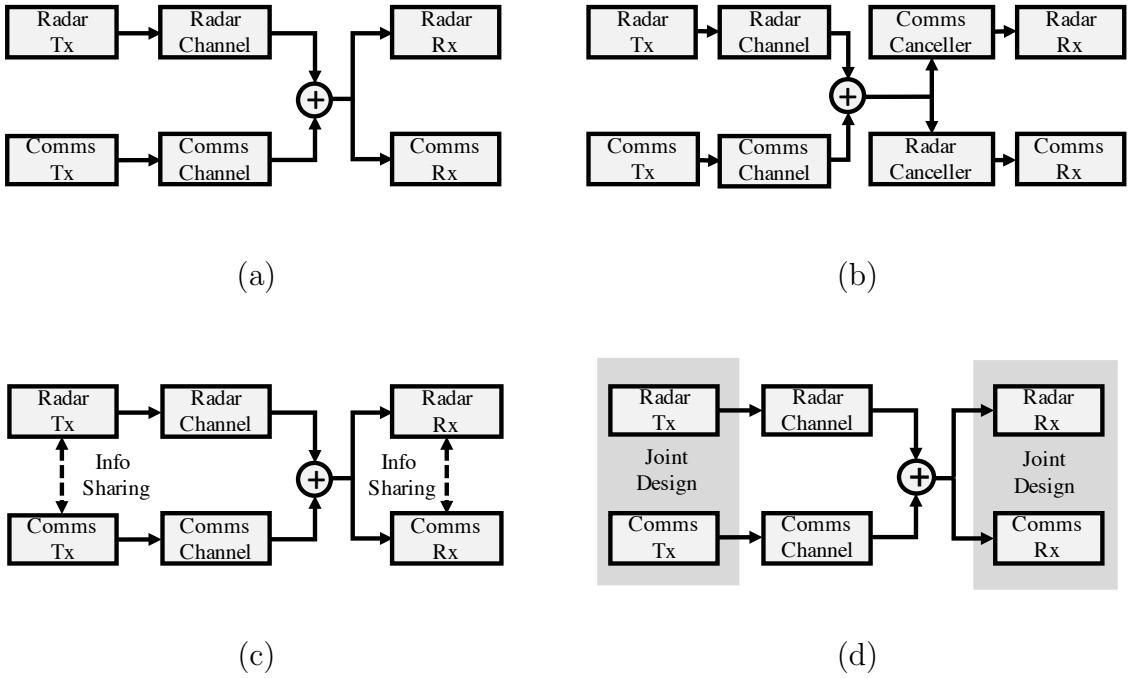

Figure 3.1: The system design concepts of the joint sensing and communications problem include isolation, coexistence, cooperation, and co-design. Isolation refers to a system in which radar and communication functions are designed independently. Coexistence refers to a system where where communication and radar functions mitigate interference from one another. Cooperaion refers to a system where information is shared between radar and communications functions allowing for mutually increased performance. Finally, co-design refers to a system where communications and radar functions are optimized in the design process.

nication mechanism exists between the radar and communications nodes [3]. As a result, any information needed to perform mitigation must be estimated. Adaptive interference cancellation techniques are employed at the receiver to improve performance for both functions.

The cooperation concept is similar to coexistence, however some information is shared between radar and communication nodes [3]. In this concept, each node is no longer considered a source of interference relative to one another. Instead, information is shared with both radar and communications nodes to improve performance. For

example, knowledge of the radar waveform can be used to assist in channel estimation and equalization for the communications node.

Finally, co-design refers to the concept of designing a transceiver node to perform both radar and communications functions jointly. In this regime both radar and communication functions are optimized jointly during the design process [3]. Various codes, modulation schemes, and training sequences can be chosen that mutually benefit radar and communications functions. The co-design process truly embodies the concept of RF convergence.

3.2 Two-Node System Topologies

There are numerous system topologies that can benefit from radio frequency (RF) convergence. For a two node system however, a representative subset of the system topologies can be grouped into the following categories [3]: joint multiple access, monostatic broadcast, bi-static broadcast, and the in-band full-duplex. Each of these system topologies are illustrated in Figure 3.2.

The joint multiple access system topology consists of a joint transceiver node that functions as a monostatic radar and communications receiver. The second node is an independent communications transmitter. The communications receiver can exploit knowledge of the known radar waveform for purposes of channel estimation and equalization. Assuming the joint transceiver node is tracking a target, successive interference cancellation (SIC) can be employed to subtract off a predicted radar return to improve communications performance. Finally, the communications transmitter can operate at a higher rate when the radar transceiver is not in use [3].

The monostatic broadcast system topology consists of a joint transceiver node that functions as a monostatic radar and communications transmitter. The second node is an independent communications receiver. Unlike the joint multiple access

channel, the two nodes now share a common waveform. Ideally, the waveform would be optimized to benefit both communications and radar functions.

The bi-static broadcast system topology consists of two joint transceiver nodes that perform both radar and communications functions. However, each node operates solely as a transmitter or a receiver. Similar to the monostatic broadcast channel topology, the two nodes are tightly coupled by a common waveform. The in-band full-duplex channel topology is bi-static in nature, but now each transceiver node operates in full duplex mode. That is, one node simultaneously operates (within the same band) as a radar transmitter and communications receiver and vice versa.

3.3 Theoretical Performance Bounds and Metrics

To properly characterize a joint sensing and communications system, compatible performance metrics must be developed. Radar performance can be characterized with an information theoretic metric known as the estimation rate [39, 68, 69], which measures the amount of information learned by illuminating a target. Communications performance can be characterized by the communications rate capacity. The communications channel capacity is the supremum of achievable communications rates for a given channel model with respect to the input distribution. This problem was solved by Shannon in his seminal work [37]. With these metrics, standard performance bounds can be recreated with joint users.

3.3.1 Communications Channel Capacity and Estimation Information Rate

The joint multiple access system topology shown in Figure 3.2 (a) is considered. One transceiver node operates as a monostatic tracking radar, while simultaneously receiving messages from an independent communications transmitter. For a single

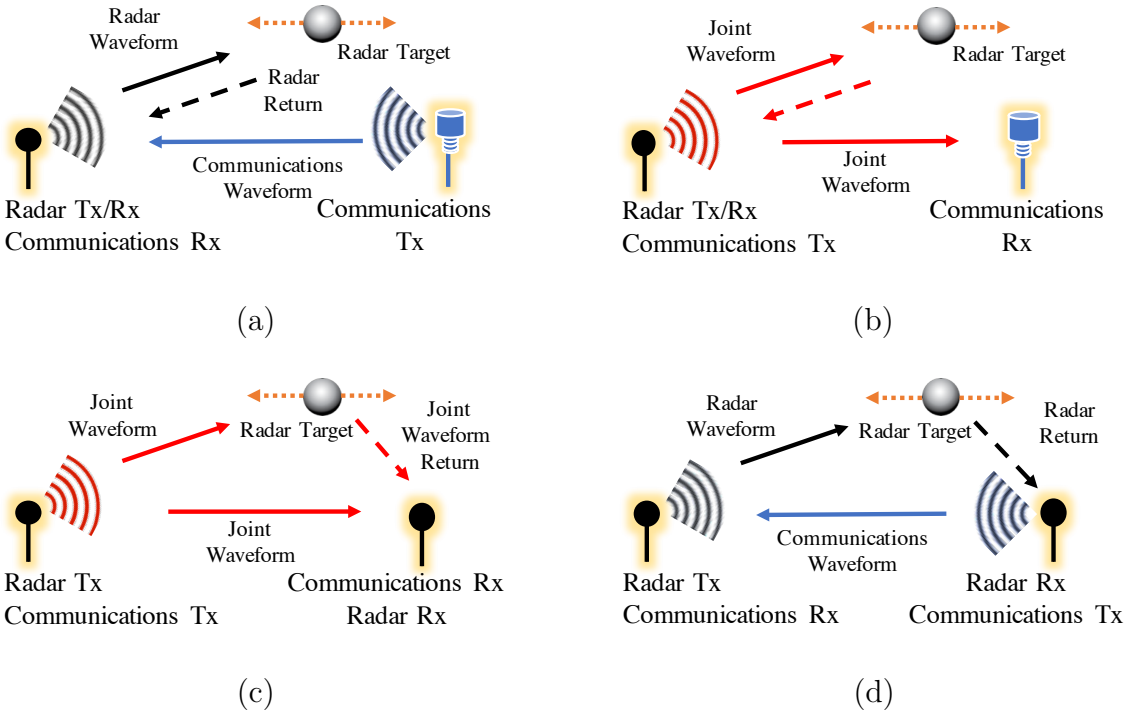

Figure 3.2: A representative set of system topologies that can benefit from RF convergence. (a) The joint multiple access system topology consists of a joint transceiver node that performs both radar and communications functions and an independent communications transmitter node. (b) The monostatic broadcast system topology consists of a joint transceiver node that performs both radar and communications functions and an independent communications receiver node. (c) The bi-static broadcast system topology consists of two joint transceiver nodes that performs both radar and communications functions. (d) The in-band full-duplex channel topology is bi-static in nature, but now each transceiver node operates in full duplex mode.

target, the received baseband signal model is

$$\underline{\mathbf{z}} = \underline{\mathbf{z}}_{\text{rad}} + \underline{\mathbf{z}}_{\text{com}} \tag{3.1}$$

$$= \sqrt{P_{\text{rad}}}\,\underline{\mathbf{x}}_{\text{rad}} * \underline{\mathbf{a}} + \sqrt{P_{\text{com}}}\,\underline{\mathbf{x}}_{\text{com}} * \underline{\mathbf{b}} + \underline{\mathbf{n}}, \tag{3.2}$$

where $\underline{\mathbf{x}}_{\text{rad}} \in \mathbb{C}^{1\times N}$ and $\underline{\mathbf{x}}_{\text{com}} \in \mathbb{C}^{1\times N}$ denote the radar return and communications row vectors, respectively. The '$*$' operator denotes convolution and the composite waveform row vector is denoted by $\underline{\mathbf{z}} \in \mathbb{C}^{1\times 2N-1}$. The radar and communications channel attenuation row vectors are denoted by $\underline{\mathbf{a}} \in \mathbb{C}^{1\times L}$ and $\underline{\mathbf{b}} \in \mathbb{C}^{1\times L}$, respectively. The channel attenuation coefficients collectively represent losses due to multi-path,

shadowing, path-loss etcetera. Finally, $\underline{\mathbf{n}} \in \mathbb{C}^{1\times 2N-1}$ denotes zero mean thermal noise row vector drawn from a complex Gaussian distribution with variance $\sigma^2_{\text{noise}} = k_{\text{B}}\, T_{\text{temp}}\, B$.

In general, the communications channel capacity for two communications nodes is given by

$$R_{\text{com}} \leq B\, \log_2\left(1 + \frac{\|\underline{\mathbf{b}}\|^2\, P_{\text{com}}}{k_{\text{B}}\, T_{\text{temp}}\, B}\right), \tag{3.3}$$

$$\leq B\, \log_2(1 + \text{SNR}), \tag{3.4}$$

where k_{B} denotes the Boltzmann constant in Joules/Kelvin and T_{temp} denotes the absolute temperature in Kelvin [70]. The variables B and P_{com} denote the available bandwidth in Hertz and total communications transmit power, respectively.

In a joint multiple access system topology, the receiver can improve communications performance by suppressing the predicted radar return from the composite waveform through a process called SIC. After suppression, the composite waveform is expressed as

$$\tilde{\underline{\mathbf{z}}} = \underline{\mathbf{r}} + \sqrt{P_{\text{com}}}\, \underline{\mathbf{x}}_{\text{com}} * \underline{\mathbf{b}} + \underline{\mathbf{n}} \tag{3.5}$$

$$\underline{\mathbf{r}} = \sqrt{P_{\text{rad}}}\, \underline{\mathbf{x}}_{\text{rad}} * \underline{\mathbf{a}} - \sqrt{\hat{P_{\text{rad}}}}\, \hat{\underline{\mathbf{x}}}_{\text{rad}} * \hat{\underline{\mathbf{a}}}, \tag{3.6}$$

where $\underline{\mathbf{r}}$ denotes the residual energy of the radar waveform after cancellation, $\hat{\mathbf{a}}$ denotes the estimated channel attenuation vector, and $\sqrt{\hat{P_{\text{rad}}}}\, \hat{\underline{\mathbf{x}}}_{\text{rad}} * \hat{\underline{\mathbf{a}}}$ denotes the predicted radar return. The communications rate after factoring in the residual term is given by [39]

$$R_{\text{com;SIC}} \leq B\, \log_2\left(1 + \frac{\|\underline{\mathbf{b}}\|^2\, P_{\text{com}}}{k_{\text{B}}\, T_{\text{temp}}\, B + P_{\text{rad}}\, \|\underline{\mathbf{a}}\|^2\, \langle \|\underline{\mathbf{r}}\|^2 \rangle}\right), \tag{3.7}$$

$$\leq B\, \log_2\left(1 + \text{SINR}\right) \tag{3.8}$$

where $\langle \cdot \rangle$ denotes the expectation function and SINR denotes the signal-to-interference plus noise ratio. Naturally, the communications rate capacity is the same as Equation (3.4) if the target track is modeled well. That is, the residual energy is small ($\langle \|\mathbf{r}\|^2 \rangle \approx 0$). These metrics hold true for the sole communications node in the scenario. However, an alternative method of information rate must be formulated for the radar node to cast it in this multi-user bound.

The information theoretic rate used to describe radar tracking performance is the estimation rate. It is defined as the mutual information between the noiseless and noisy target tracking state per unit time [71]:

$$R_{\text{est}} = \frac{I(X;Y)}{T}, \tag{3.9}$$

where $I(X;Y)$ is the mutual information between the noiseless state measurement X and the noisy state measurement Y over the revisit period T. For pulsed radar operation, the pulse repetition interval (T_{pri}) can be interchanged with the revisit period. In this work, the receiver generates a predicted radar return by tracking the range and range-rate of a target using the Kalman filter [72]; within this framework, the derivation of Equation (3.9) arises naturally [39, 71].

In this formulation, the target velocity is assumed constant and the underlying target motion is accurately modeled by a two-dimensional (2D) linear motion model with Gaussian perturbation acceleration [73]:

$$\mathbf{s}_k = \mathbf{A}\,\mathbf{s}_{k-1} + \mathbf{q}_{k-1} \tag{3.10}$$

$$= \begin{bmatrix} 1 & T \\ 0 & 1 \end{bmatrix} \begin{bmatrix} R_{k-1} \\ \dot{R}_{k-1} \end{bmatrix} + \mathbf{q}_{k-1} \tag{3.11}$$

where the dynamic states R_{k-1} and $\dot{R}_{k-1}$ are the range and range-rate at time step $k-1$. The variable $\mathbf{q}_{k-1} \sim \mathcal{N}(\mathbf{0}, \mathbf{Q}_{k-1})$ denotes the process noise at time step $k-1$

with covariance matrix

$$\mathbf{Q}_k = q_k \begin{bmatrix} \frac{T^3}{3} & \frac{T^2}{2} \\ \frac{T^2}{2} & T \end{bmatrix}, \tag{3.12}$$

where q_k denotes the process model error intensity.

The receiver measurements include the estimated range R_k and range-rate $\dot{R}_k$ of the target. We assume a narrowband environment [74, 75] $T\,B \ll c/(2\,\dot{R}_k)$, where c denotes the speed of light, such that the receiver observes only the Doppler shift in the radar return. Under this assumption, the measurement model is:

$$\mathbf{y}_k = \mathbf{H}\,\mathbf{s}_k + \mathbf{r}_k \tag{3.13}$$

$$= \begin{bmatrix} 1 & 0 \\ 0 & 1 \end{bmatrix} \begin{bmatrix} R_k \\ \dot{R}_k \end{bmatrix} + \mathbf{r}_k, \tag{3.14}$$

where $\mathbf{r}_k \sim \mathcal{N}(\mathbf{0}, \mathbf{R}_k)$ denotes the measurement noise at time step k.

With this formulation the estimation rate of the target is given by [39, 76]

$$R_{\text{est}} \leq \frac{1}{2\,T}\,\log_2\!\left(\frac{|\mathbf{S}_k|}{|\mathbf{R}_k|}\right) \tag{3.15}$$

$$\mathbf{S}_k = \mathbf{H}\,\mathbf{P}_{k|k-1}\,\mathbf{H}^\dagger + \mathbf{R}_k \tag{3.16}$$

$$\mathbf{P}_{k|k-1} = \mathbf{A}\,\mathbf{P}_{k-1}\,\mathbf{A}^\dagger + \mathbf{Q}_{k-1}, \tag{3.17}$$

where $|\cdot|$ and † denote the determinant function and Hermitian transpose. The variable $\mathbf{P}_{k|k-1}$ denotes the predicted model covariance, $\mathbf{S}_k$ denotes the measurement prediction covariance, and $\mathbf{R}_k$ is the measurement noise covariance. Equation (3.15) represents the minimum number of bits needed to encode the Kalman residual, which is the statistical deviation from the radar prediction of the target parameters, for a given channel [2, 77].

The estimation rate for a joint multiple access system topology retains the same form as in Equation (3.15). This holds true under the assumption that the receiver

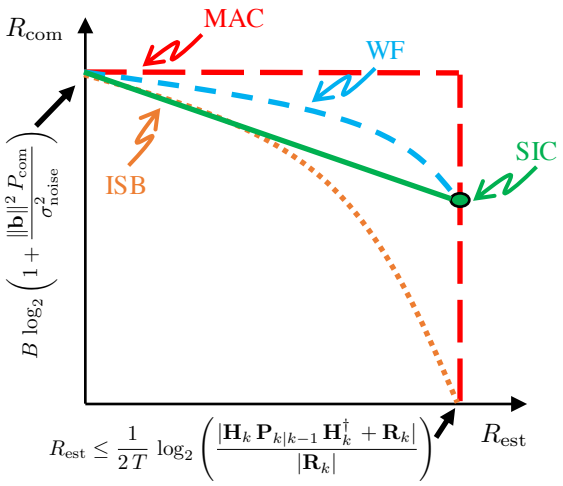

Figure 3.3: Example joint radar communications multiple access achievable rate region. SIC is no longer achievable when the communications user is operating at capacity because the radar return cannot be estimated perfectly and therefore leaves a residual when subtracted. The isolated sub-band (ISB) bound isolates the two users in separate fractions of the system bandwidth. The SIC bound time averages between the SIC point with reduced comms and full comms with no radar. The water filling (WF) bound applies a traditional water filling approach to these same two points [78].

node is operating at a reduced rate to handle the increase in noise and interference. As such, the communications waveform can be decoded as perfectly as possible and subtracted from the composite. Thus allowing for the radar return to be processed with little interference.

3.3.2 Joint Multiple Access Performance Bounds

With the radar estimation information rate defined, one can characterize the performance of a joint sensing and communications system using traditional multiple access techniques [70]. In Figure 3.3, a notional example of various bounds on performance that arise from the joint multiple access system topology is presented. These bounds are reviewed here, and a more detailed discussion and derivation is provided in Reference [2].

The multiple access channel (MAC) bound is the intersection of the estimation and communications performance points when the radar and communications nodes operate in isolation. This bound is the theoretically best, albeit unachievable, bound for when the nodes operate for a given spectrum-space-time access. The isolated sub-band (ISB) bound is indicative of system performance when the radar and communications node operate within separate fractions of the allocated bandwidth. A blending ratio, α, controls the amount of bandwidth allocated to the communications and radar node. As the fraction of total bandwidth $(1 - \alpha)$ allocated for radar operation is increased, radar parameter estimation also increases. However, the communications rate decreases. The receiver performs radar and communications processing on their respective individual channels. The ISB system is representative of current solutions for radar and communications operation. A notional illustration of the bandwidth allocation concept for the ISB scenario is illustrated in Figure 3.4 (a).

The communications water-filling (WF) bound is achieved in similar fashion as the ISB bound, but the communications transmitter splits the bandwidth into a communications-only, and mixed use sub-band. The receiver does interference free decoding in the communications-only sub-band, and uses SIC to decode the communications and radar information in the mixed use sub-band. A notional illustration of the bandwidth allocation concept for the communications WF scenario is illustrated in Figure 3.4 (b).

The SIC point represents operating point of the system for a mixed use channel when SIC is employed. The SIC bound is achieved by time averaging between communications-only and mixed use operation. While there appears to be a linear decrease in estimation rate, for any given radar spectrum-space-time access, the radar is operating over the entire allocated bandwidth, unimpeded by the communications user.

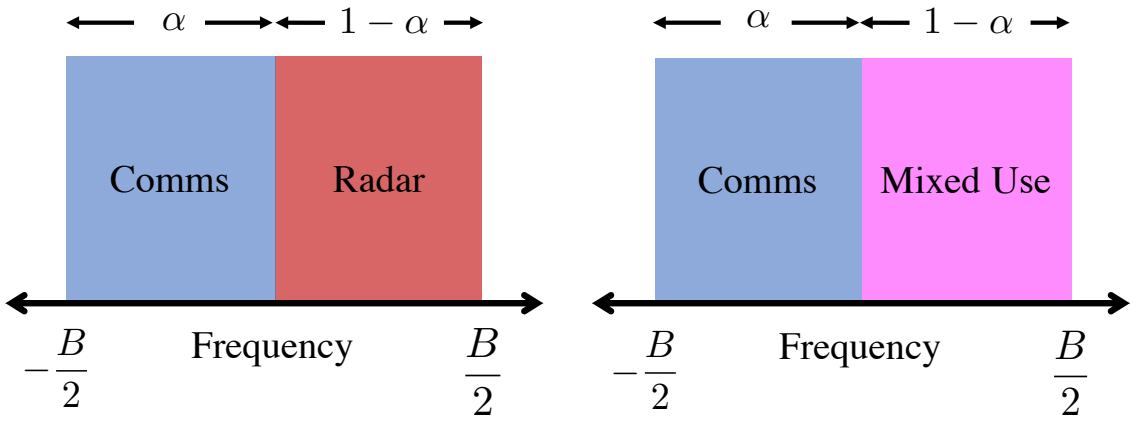

Figure 3.4: Notional illustration of ISB and communications water-filling (WF) bandwidth allocation. For a given bandwidth B, the bandwidth is split into two sub-bands based on a split factor α. For ISB, one sub-band is utilized for communications and the other is used for radar. The receiver architecture processes the communications and radar waveforms separately. For communications WF, one sub-band is utilized for communications and the other is mixed use. Successive interference cancellation techniques are employed in the mixed use band to separate both radar and communications waveforms for processing.

Chapter 4

JOINT MULTIPLE ACCESS SDR RECEIVER ARCHITECTURE

In Chapter 3, the various joint sensing and communication system design concepts were introduced. Additionally, representative two-node system topologies were discussed. Finally, the theoretical performance metrics and the successive interference cancellation (SIC) bound that arises within a joint multiple access system topology was presented. In this chapter, a discussion of various receiver architectures is presented. Additionally, discussions of the SDR architecture implementations are provided. Finally an analysis of the experimental performance for each system is provided. An early version of this research thread is presented in Reference [44].

4.1 Joint Multiple Access Receiver Design

Recall that the complex baseband model for the received composite waveform for a single target is

$$\underline{\mathbf{z}} = \underline{\mathbf{z}}_{\text{rad}} + \underline{\mathbf{z}}_{\text{com}} \tag{4.1}$$

$$= \sqrt{P_{\text{rad}}}\,\underline{\mathbf{x}}_{\text{rad}} * \underline{\mathbf{a}} + \sqrt{P_{\text{com}}}\,\mathbf{x}_{\text{com}} * \underline{\mathbf{b}} + \underline{\mathbf{n}}, \tag{4.2}$$

where the associated variables denote the same quantities described in Equation (3.2). Using this model, the signal processing chain for the joint multiple access receiver discussed in this work is divided into three stages:

1. Generate a predicted radar return, $\hat{\underline{\mathbf{x}}}_{\text{rad}}$, using previous state information, filter it with an estimate of the radar channel, $\hat{\underline{\mathbf{a}}}$, and subtract it from the composite waveform $\underline{\mathbf{z}}$;

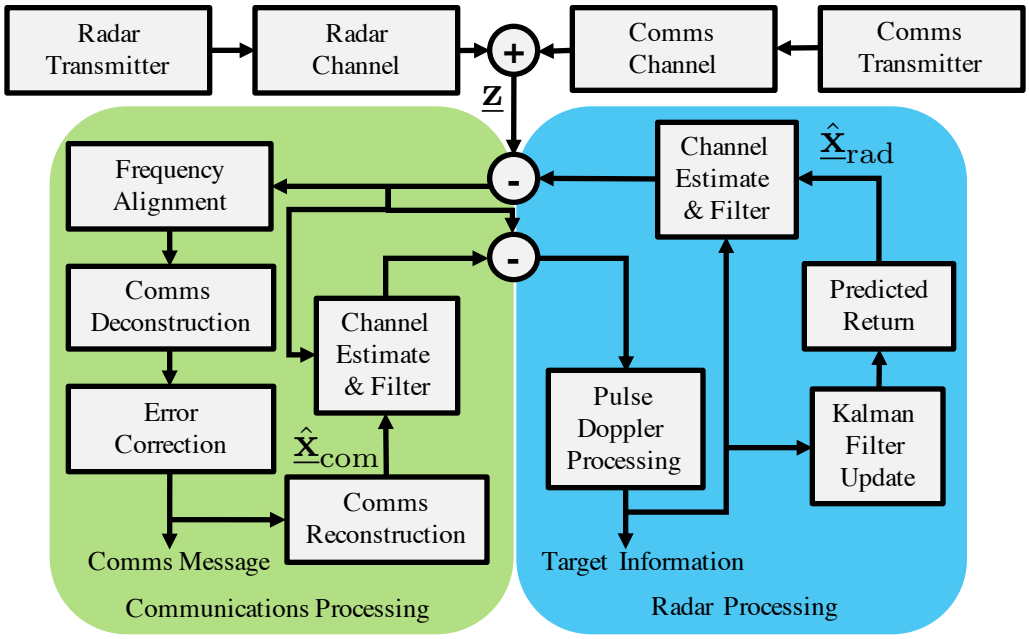

Figure 4.1: Joint multiple access receiver architecture for SIC scenario. The radar and communications signals have two effective channels, but arrive converged at the joint receiver. The radar signal is predicted and removed, allowing a reduced rate communications user to operate. Assuming near perfect decoding of the communications user, the ideal signal can be reconstructed and subtracted from the original waveform, allowing for unimpeded radar access.

2. Generate an estimate of the transmit waveform, $\hat{\underline{\mathbf{x}}}_{\text{com}}$, filter with communications channel estimate, $\hat{\underline{\mathbf{b}}}$, and subtract it from the composite waveform;

3. Process the radar return using radar processing techniques.

The block diagram representation of the co-design receiver architecture is shown in Figure 4.1.

4.1.1 Communications Signal Processing

The communications signal processing chain is divided into five steps:

1. removal of predicted radar return

2. coarse frequency alignment and matched filtering,

3. communications waveform deconstruction,

4. communications waveform reconstruction,

5. communications waveform mitigation.

Suppression of the predicted radar return can be performed using time or spatial domain techniques [42]. For time domain techniques, suppression is performed by generating a predicted radar return using the previous states (predicted range and range-rate) estimate and subtract it from the composite. In the spatial domain, radar suppression is accomplished by projecting the composite waveform into an orthogonal basis spanned by the predicted radar return. Here, a time domain technique is employed.

Coarse frequency alignment is performed using a maximum likelihood (ML) estimator [48]. A minimum mean squared error (MMSE) Wiener filter is constructed using the communications pilot sequence and applied to the composite waveform to extract the communications component. The output of this matched filter is deconstructed and the resulting symbols are decoded to produce the final estimate of the communications message bits. The message bits are then reconstructed to produce an estimate, $\hat{\underline{\mathbf{x}}}_{\text{com}}$, of the original transmitted waveform. This waveform is subtracted from the composite using the same process employed for radar suppression. Images of a single pulse for a linear frequency modulated waveform before and after the communications waveform mitigation step for the SIC process are presented in Figure 4.2.

4.1.2 Radar Signal Processing

Pulse-Doppler processing techniques are employed to extract Doppler and range estimates from the radar return. It is assumed that Doppler is not resolvable by a single pulse, thus matched filtering is applied across K coherent pulses for both range

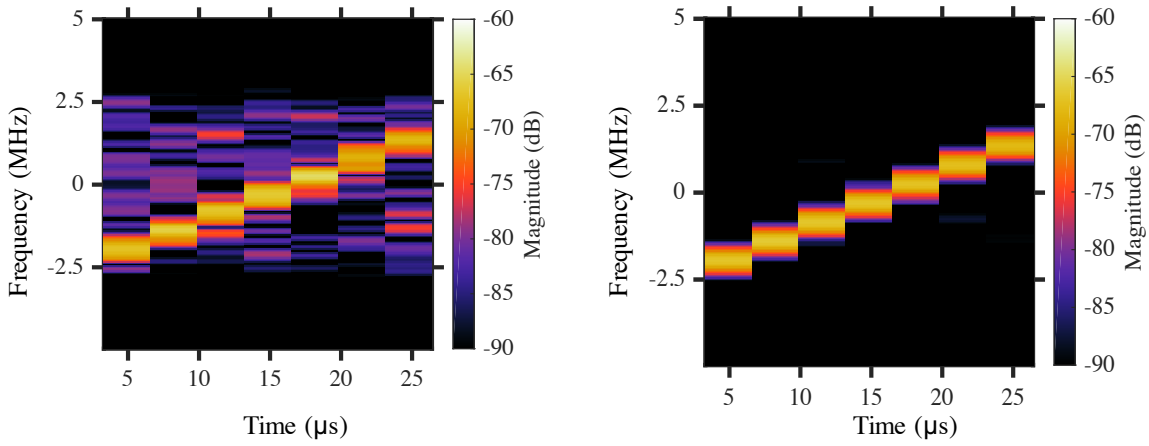

(a) (b)

Figure 4.2: Images of a recorded single pulse for a linear frequency modulated waveform before and after the communications waveform mitigation step for the SIC process. Both the radar and communications waveform appear in the composite waveform shown in (a). The resulting waveform of the communications waveform mitigation step is shown in (b). The communications waveform residual is very small which produces a high resolution radar return.

and Doppler hypotheses. Elements of the range-Doppler matrix, $\mathbf{A} \in \mathbb{C}^{M \times K}$, are computed as

$$\{\mathbf{A}\}_{m,k} = \frac{1}{N} \sum_{n=0}^{N-1} \{\underline{\mathbf{x}}_{\text{lfm}}\}^*_{n+m} \{\underline{\mathbf{z}}\}_n \exp\left(\frac{-j\,2\,\pi\,k\,n}{N}\right), \tag{4.3}$$

where N is the integration length, $m \in \{-M, \ldots, M\}$ is the range index, $k \in \{-\frac{K}{2}, \ldots, \frac{K}{2} - 1\}$, denotes the Doppler index, and $\underline{\mathbf{x}}_{\text{lfm}}$ denotes the transmitted radar waveform. A coarse estimate of the Doppler and range indices of the target is

$$\left\{\hat{m},\, \hat{k}\right\} = \arg\max_{m,\,k} \{\mathbf{A}\}_{m,k} \tag{4.4}$$

This process is illustrated in Figure 4.3.

Higher resolution range and Doppler estimates are produced using sinc interpolation techniques within the range-Doppler bin:

$$\{\boldsymbol{\mathcal{A}}\}_{i,j} = \sum_{i=-I}^{I} \sum_{j=-J}^{J} \{\mathbf{A}\}_{\hat{m},\hat{k}} \operatorname{sinc}_2\left(\frac{\hat{m} - i\,\Delta_m}{\Delta_m}, \frac{\hat{k} - j\,\Delta_k}{\Delta_k}\right), \tag{4.5}$$

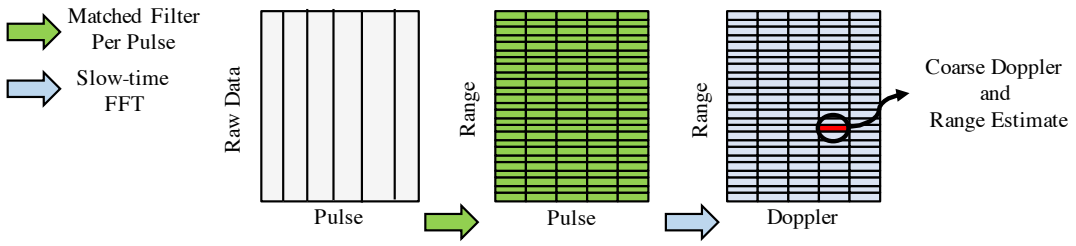

Figure 4.3: Pulse-Doppler processing is used to obtain coarse Doppler and range estimates of the target. The coarse target estimate is computed by performing matched filtering across both delay and frequency. The indices of the maximum value for delay and frequency correspond to the coarse estimate of the relative range and Doppler. Interpolation techniques are then applied in order to obtain better estimation resolution.

where sinc_2[1] denotes the two dimensional sinc function, Δm and Δk denotes the interpolated spacing factors for range and Doppler, $\{\boldsymbol{\mathcal{A}}\}_{i,j}$ denotes the row/column element pair of the interpolated range-Doppler bin matrix, $\{I, J\} \in \mathbb{Z}$ denote the integer number of bins around the maximum value to interpolate. The final range and range-rate estimates are computed by choosing the maximum within the new matrix as follows

$$\{\hat{i}, \hat{j}\} = \arg\max_{i,j} \{\boldsymbol{\mathcal{A}}\}_{i,j} \tag{4.6}$$

$$\hat{R} = \frac{\hat{i}\, c}{2\, f_{\text{s}}} \tag{4.7}$$

$$\hat{\dot{R}} = \frac{(\hat{j} - j_0)\, \lambda}{2\, T_{\text{pri}}\, K} \tag{4.8}$$

where f_{s} (samples/second) is the digital-to-analog converter sampling rate and $\lambda = c/f_{\text{c}}$ is the wavelength (meters), j_0 denotes the zero doppler bin index, and T_{pri} denotes the pulse repetition interval.

[1] $\text{sinc}_2\left(\frac{x}{\Delta x}, \frac{y}{\Delta y}\right) = \text{sinc}\left(\frac{x}{\Delta x}\right) \text{sinc}\left(\frac{y}{\Delta y}\right)$

4.1.3 Kalman Filter Target Tracking

The receiver utilizes the Kalman filter to track the range and range-rate of the target. The Kalman filter provides a state-space solution to the Wiener problem [72] — it generates new predictions using previous state estimates based on a physical model and updates the current state estimates using measurements of these states. The Kalman filter accomplishes this via the following steps [72]:

- *Prediction*

$$\mathbf{s}_{k|k-1} = \mathbf{A}\,\mathbf{s}_{k-1} \tag{4.9}$$

$$\mathbf{P}_{k|k-1} = \mathbf{A}\,\mathbf{P}_{k-1}\,\mathbf{A}^T + \mathbf{Q}_{k-1} \tag{4.10}$$

- *Update*

$$\mathbf{R}_k = \beta\,\mathbf{R}_{k-1} + (1-\beta)\,\mathbf{H}\,\mathbf{P}_{k|k-1}\,\mathbf{H}^T \tag{4.11}$$

$$\mathbf{K}_k = \mathbf{P}_{k|k-1}\,\mathbf{H}^T\,(\mathbf{H}\,\mathbf{P}_{k|k-1}\,\mathbf{H}^T + \mathbf{R}_k)^{-1} \tag{4.12}$$

$$\mathbf{v}_k = \mathbf{y}_k - \mathbf{H}\,\mathbf{s}_{k|k-1} \tag{4.13}$$

$$\mathbf{Q}_k = \eta\,\mathbf{Q}_{k-1} + (1-\eta)\,(\mathbf{K}_k\,(\mathbf{v}_k\,\mathbf{v}_k^T)\,\mathbf{K}_k) \tag{4.14}$$

$$\mathbf{s}_k = \mathbf{s}_{k|k-1} + \mathbf{K}_k\,\mathbf{v}_k \tag{4.15}$$

$$\mathbf{P}_k = \mathbf{P}_{k|k-1} - \mathbf{K}_k\,(\mathbf{H}\,\mathbf{P}_{k|k-1}\,\mathbf{H}^T + \mathbf{R}_k)\,\mathbf{K}_k^T \tag{4.16}$$

where the quantity $\mathbf{v}_k$ is the innovation or measurement residual at time step k, β and η denote forgetting factors for the measurement and process covariance at time step $k-1$, and $\mathbf{K}_k$ is the filter gain (how much the predictions should be corrected) at time step k. The forgetting factors allow for adaptive adjustment of the initial error covariance estimates [79].

4.2 Receiver Architecture Variations

As discussed in Section 3.3, variations of the joint multiple access system implementations result in different bounds on system performance. For the ISB system, the transmitters employ a complex phase ramp to shift both the communications and radar waveforms off of the carrier frequency

$$\underline{\mathbf{x}}_{\text{com;tx}} = \sqrt{P_{\text{com}}}\, \exp\left\{\frac{j\,2\,\pi\,f_1}{f_s}\,\underline{\mathbf{m}}\right\} \odot \underline{\mathbf{x}}_{\text{com}} \tag{4.17}$$

$$\underline{\mathbf{x}}_{\text{rad;tx}} = \sqrt{P_{\text{rad}}}\, \exp\left\{\frac{j\,2\,\pi\,f_2}{f_s}\,\underline{\mathbf{m}}\right\} \odot \underline{\mathbf{x}}_{\text{rad}} \tag{4.18}$$

$$\underline{\mathbf{m}} = \begin{bmatrix} 0 & 1 & \dots & N-1 \end{bmatrix}, \tag{4.19}$$

where f_1 and f_2 denotes the carrier frequency offset for the communications and radar waveforms and P_{com} denotes the transmitted communications waveform power. The receiver employs a *channelizer*, which consists of a frequency shift and low pass filter, to split the received waveform into a communications and radar channel. The receiver processes these two channels to extract the communications message and target information independently. The receiver architecture for the ISB system is illustrated in Figure 4.4 (a).

A similar architecture is employed in the communications WF system. As with the ISB system, the transmitters employ a complex phase ramp to split the allocated bandwidth into two sub-bands. The communications transmitter emits a waveform which consists of the concatenation of two

$$\underline{\mathbf{x}}_{\text{com;tx}_1} = \sqrt{P_{\text{com;tx}_1}}\, \exp\left\{\frac{j\,2\,\pi\,f_1}{f_s}\,\underline{\mathbf{m}}\right\} \odot \underline{\mathbf{x}}_{\text{com}_1} \tag{4.20}$$

$$\underline{\mathbf{x}}_{\text{com;tx}_2} = \sqrt{P_{\text{com;tx}_2}}\, \exp\left\{\frac{j\,2\,\pi\,f_2}{f_s}\,\underline{\mathbf{m}}\right\} \odot \underline{\mathbf{x}}_{\text{com}_2} \tag{4.21}$$

$$\underline{\mathbf{x}}_{\text{com;tx}} = \begin{bmatrix} \underline{\mathbf{x}}_{\text{com;tx}_1} & \underline{\mathbf{x}}_{\text{com;tx}_2} \end{bmatrix}, \tag{4.22}$$

where $\underline{\mathbf{x}}_{\text{com;tx}_1}$ and $\underline{\mathbf{x}}_{\text{com;tx}_2}$ denote the communications waveforms for the communications only sub-band and mixed use sub-band. The variables f_1 and f_2 denote the frequency offsets for each sub-band. Similarly, the radar transmitter

$$\underline{\mathbf{x}}_{\text{rad;tx}} = \sqrt{P_{\text{rad}}}\, \exp\left\{ \frac{j\, 2\, \pi\, f_2}{f_s}\, \underline{\mathbf{m}} \right\}\, \underline{\mathbf{x}}_{\text{rad}} \tag{4.23}$$

employs the same frequency shift f_2 as the mixed use sub-band communications waveform $\underline{\mathbf{x}}_{\text{com;tx}_2}$.

The receiver observes the composite waveform

$$\begin{aligned} \underline{\mathbf{z}} &= \underline{\mathbf{z}}_{\text{com;tx}} + \underline{\mathbf{z}}_{\text{rad;tx}} \\ &= \underline{\mathbf{x}}_{\text{com;tx}} * \underline{\mathbf{b}} + \underline{\mathbf{x}}_{\text{rad;tx}} * \underline{\mathbf{a}} + \underline{\mathbf{n}}, \end{aligned} \tag{4.24}$$

which is separated by the channelizer into the mixed use sub-band

$$\begin{aligned} \underline{\mathbf{z}}_{\text{mix}} &= \underline{\mathbf{z}}_{\text{com}_2} + \underline{\mathbf{z}}_{\text{rad}} \\ &= \underline{\mathbf{x}}_{\text{com}_2} * \underline{\mathbf{b}} + \underline{\mathbf{x}}_{\text{rad}} * \underline{\mathbf{a}} + \underline{\mathbf{n}} \end{aligned} \tag{4.25}$$

and the communications only sub-band

$$\underline{\mathbf{z}}_{\text{com}_1} = \underline{\mathbf{x}}_{\text{com}_1} * \underline{\mathbf{b}}. \tag{4.26}$$

The receiver then performs interference free decoding on the communications only sub-band in Equation (4.26) and employs SIC techniques in the mixed use sub-band to extract target information from the radar and decode the communications waveform. The receiver architecture for the communications WF system is illustrated in Figure 4.4 (b).

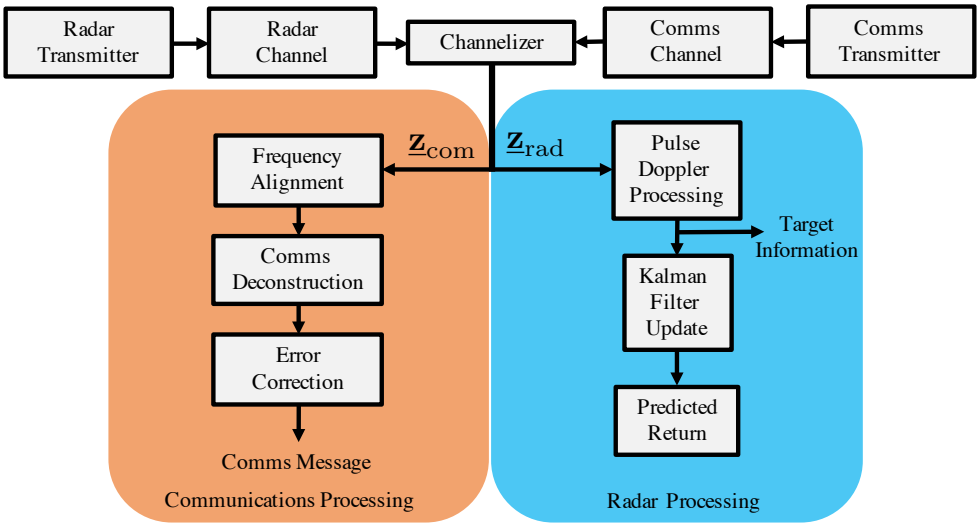

(a)

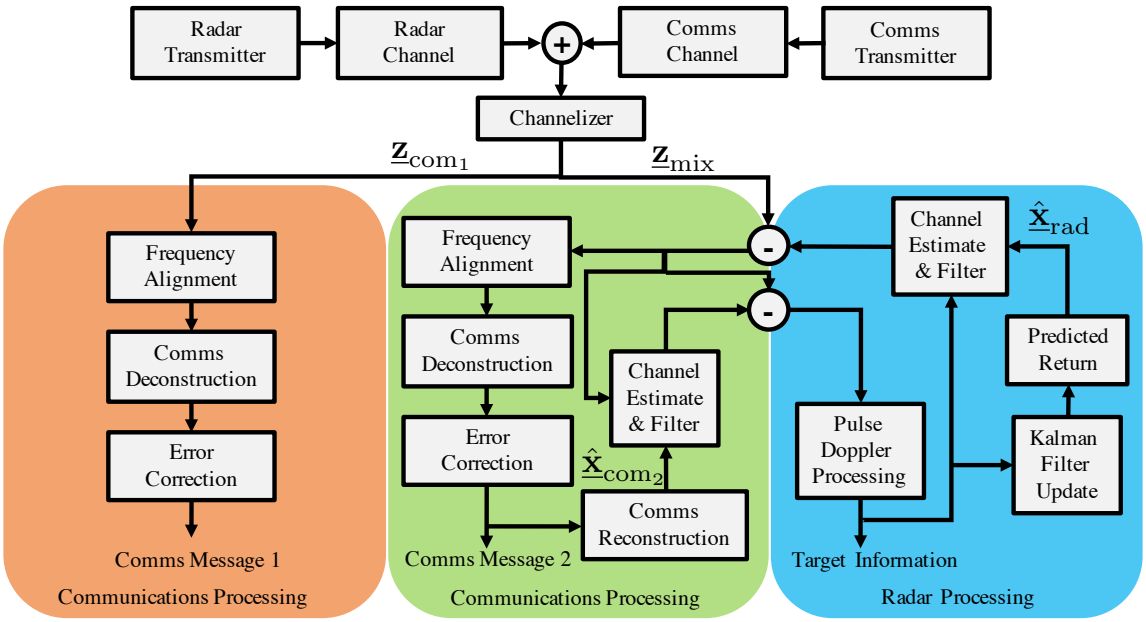

(b)

Figure 4.4: Receiver architectures for the ISB and communications WF scenarios. The transmitters employ a complex phase ramp to shift both the communications and radar waveforms off of the carrier frequency into the respective sub-bands. The receiver employs a channelizer to split the waveforms into sub-channels that are processed independently.

Chapter 5

OVER-THE-AIR EXPERIMENTS

In this chapter, the performance of the joint multiple access receiver architectures discussed in Chapter 4 are examined via over-the-air experiments. An overview of the experiments including a description of the waveforms, network testbed, and various parameters used in the experiments are presented. Further, a discussion of the results for each experiment is presented.

5.1 Experiment Overview

In the experiments, a variant of the joint multiple access system topology is implemented using a network of three software defined radio nodes. Two nodes function as independent radar and communications transmitters and emit different waveforms. The third node functions as a joint sensing and communications receiver designed using the signal processing techniques discussed in Section 4.1. The joint sensing and communications receiver along with the radar transmitter is considered to be quasi-monostatic: the transceivers are slightly separated, but still appear to be at the same location as viewed from the target. The system topology is depicted in Figure 5.1.

5.1.1 Communications and Radar Target Waveforms

The communications waveform design process begins with a binary message sequence. The message can be anything from a pseudorandom binary noise sequence or simple ASCII text message downconverted to a binary stream. The message bits are encoded using a forward error correction code. Block or convolutional codes are both acceptable and the code length can be arbitrary. For scenarios with very dispersive

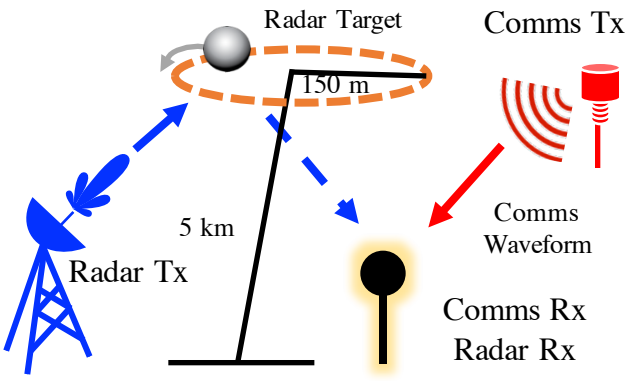

Figure 5.1: Illustration of the multiple input, single output (MISO) joint multiple access system topology implemented in the experiments. One user transmits radar waveform pulses, while a second user transmits communications waveform packets. A third user processes the radar return and received communications waveform jointly.

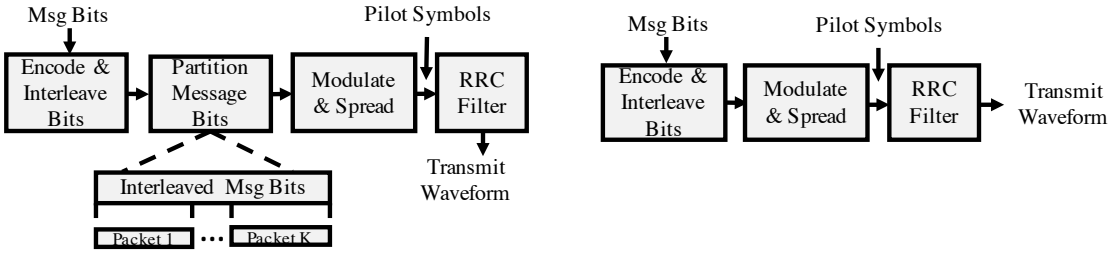

(a) (b)

Figure 5.2: The block diagram for two methods of the communications waveform generation process. (a) For very dispersive channels, a long message ($\sim$ 100 kbits) is utilized in order to generate a long error correcting code to combat channel effects. (b) In this work, a communications waveform is constructed from a small number ($\sim$ 15 kbits) of message bits. This is primarily done in order to generate a one-for-one calculation of the estimation and communications rate.

environments, such as the one considered in Reference [78, 80], a long error correction code (relative to the expected delay spread of the channel) should be utilized to combat the channel effects. For much less dispersive channels, the code length should be long enough to provide high throughput at the receiver. In this scenario, turbo coding [81] is employed. To increase robustness, block interleaving is performed on the encoded bit sequence.

In the event that a longer code is used, the encoded bit sequence is partitioned into packets. Any number of packets can be used. In general, however, it makes processing easier if the number of packets is chosen to be evenly divisible by the number of bits within the encoded bit sequence. Quadrature phase-shift keying modulation is employed to modulate the encoded packets. A Kasami spreading sequence is applied to the QPSK symbol packets. The error correction code rate is fixed, so the spreading sequence allows for intelligent data rate control at the receiver. For example, if the signal-to-noise ratio (SNR) measured at the receiver is below some specified threshold, the receiver can instruct the the transmitter to increase the spreading factor. The feedback between the receiver and transmitter is accomplished via a low data rate feedback communications link.

Before pulse-shaping, binary phase-shift keying (BPSK) modulated pilot and suffix symbols are concatenated to each packet. The final transmission waveform is achieved by filtering each symbol packet with a root-raised-cosine pulse-shaping filter. The resulting waveform is upsampled by some specified factor. A block diagram representation of the communications waveform construction for a long and short code length is shown in Figure 5.2.

A target response is emulated at the receiver by encoding a time delay and carrier frequency shift of a predefined target path into the transmission waveform. The base waveform is a linear frequency-modulated (LFM) chirp of the form

$$\{\underline{\mathbf{x}}_{\text{lfm}}\}_n = \exp\left\{\frac{j\,\pi\,B\,n^2}{T_{\text{chirp}}}\right\} \quad \text{for} \quad n = 0, 1, \ldots, N-1, \tag{5.1}$$

which is then encoded with a range and Doppler offset to obtain the final transmission waveform

$$\{\underline{\mathbf{x}}_{\text{rad}}\}_n = \{\underline{\mathbf{x}}_{\text{lfm}}\}_{n-n_R} \exp\left\{\frac{j\,4\,\pi\,\dot{R}\,f_s\,(n-n_R)}{\lambda}\right\}, \tag{5.2}$$

$$= A \exp\left\{\frac{j\,\pi\,B\,(n-n_R)^2}{T_{\text{chirp}}\,{f_s}^2} + \frac{j\,4\,\pi\,\dot{R}\,(n-n_R)}{\lambda\,f_s}\right\}, \tag{5.3}$$

$$n_R = \text{round}\left(\frac{2\,R\,f_{\text{s}}}{c}\right) \tag{5.4}$$

where T_{chirp} denotes the chirp duration, A denotes the amplitude, n_R denotes the discrete time delay index for the associated range value. The low-power nature of the target return is emulated by restricting the DAC output amplitude of the target transmitter to a value that produces a low SNR value at the receiver.

5.1.2 The WISCA SDR Network

The Center for Wireless Information Systems and Computational Architectures (WISCA) SDR Network is a suite of distributed network transceivers which users can develop and test advanced radar and wireless communications protocols. Each transceiver node in the network utilizes Ettus Research™ USRP technology. The low-level command and control software utilizes the USRP hardware driver (UHD). To provide users with a highly configurable and flexible application programming interface, baseband processing is performed within the industry standard MATLAB® algorithm development environment. As part of the implementation, low-level hardware and data management is handled automatically in the background. This decreases development time by allowing users to focus their efforts on the design and testing of algorithms. An example of the MATLAB® API is shown in Figure 5.4 (b).

The network utilizes a control/edge node structure. A single control node provides system management interface for the user. Further, the control node is responsible

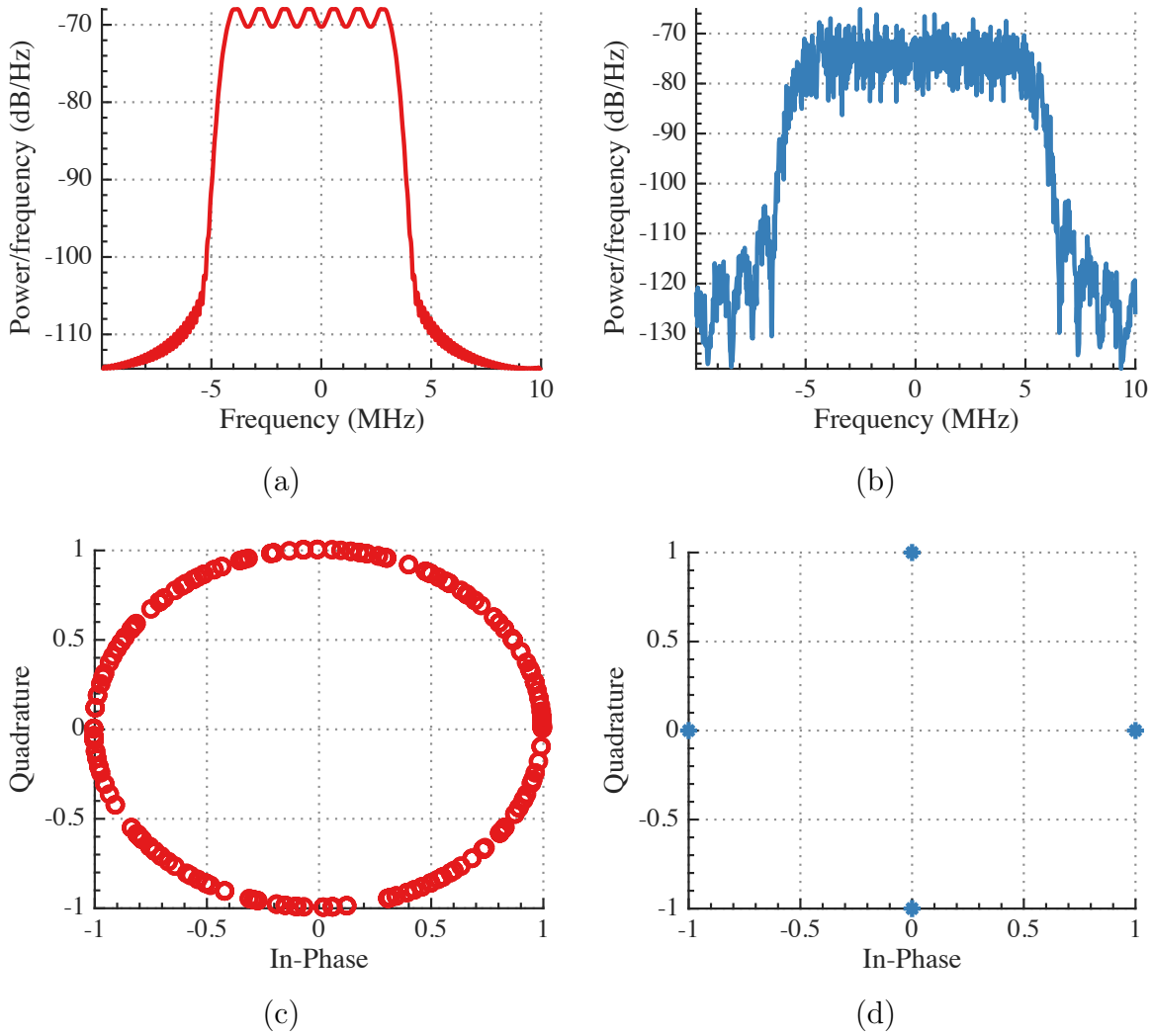

Figure 5.3: Spectrum plots of the (a) Linear frequency modulated (LFM) chirp waveform and (b) encoded QPSK waveform used in the experiments. Each waveform was approximately 10 MHz bandwidth. In-phase and quadrature diagrams for (c) the LFM chirp waveform and (d) the encoded QPSK waveform.

for distributing and executing a user's MATLAB® code, as well as collecting data from each edge node once the program ends. The edge nodes primary responsibility is executing the user's code via the customized MATLAB® USRP application programming interface (API). Each node in the network is synchronized via a GPS signal reference broadcast from a GPS repeater installed in the laboratory. The concept of operations for the network is shown in Figure 5.6.

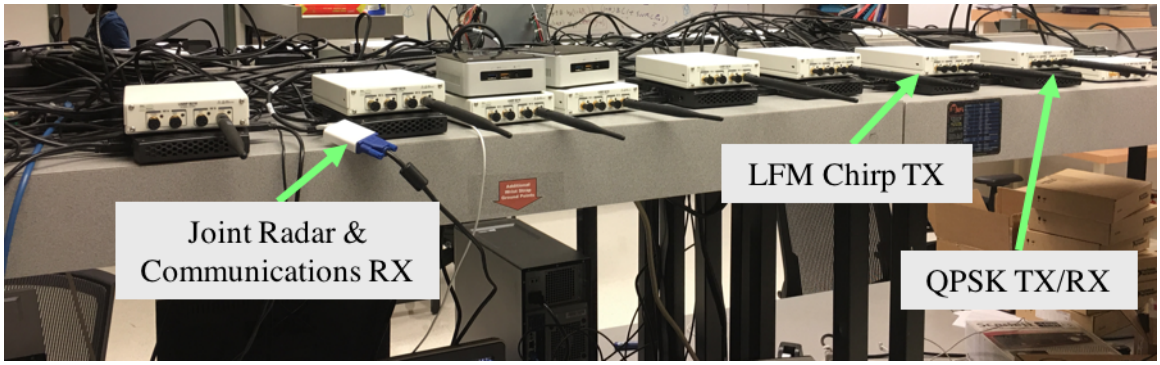

(a)

```
%------------------WISCA SDR-N API------------------
%Initial USRP and set parameters.
setusrp(radio, ant, subdev, ref, wirefmt, num_samps,
 sample_rate, freq, rx_gain, tx_gain, setup_time);
%---------------------------------------------------
%Transmit data from tx buffer based on time stamp.
tx_usrp(start_time, tx_buff);
%---------------------------------------------------
% Receive onto rx buffer based on time stamp.
rx_buff = rx_usrp(start_time);
%---------------------------------------------------
% Terminate radio object.
terminate_usrp();
%---------------------------------------------------
```

(b)

Figure 5.4: Image of the radios and laboratory environment used in the experiments. The system was implemented using the WISCA SDR Network described in [43]. A three user joint multiple access topology was implemented. Each radio node consisted of an Ettus Research^{TM} universal software radio peripheral (USRP) B-210 transceiver. (b) The MATLAB API contains four simple functions that allow the user to interact with each USRP device.

For sophisticated radio protocols, MATLAB® cannot often keep up with the required computational time needed to realize such algorithms. To bypass this limitation, the network transmits and receives data in discrete pulses and implements the user-specified processing chain in MATLAB® between pulses. This emulates continuous-time systems, but allows the processing to be done discontinuously between pulses. This process is illustrated in Figure 5.5. The processing time between

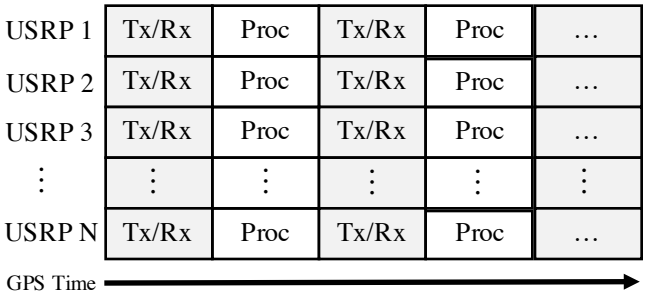

Figure 5.5: The network mimics real time operation by using discontinuous MATLAB processing and transmit/receive cycles. During a transmit/receive cycle, the USRP devices transmit or receive data, while MATLAB remains idle. During a processing cycle, the radios stop transmitting/receiving and the MATLAB script processes the data.

pulses is variable and is configurable by the user. An illustration of this processing concept is shown in Figure 5.5 (a).

5.1.3 Experiment Parameters

A pseudorandom sequence of 15 Kbits was generated for the communications message with a total of 200 messages transmitted for the duration of the experiment After turbo encoding, the length of each message increased to 75018 bits. QPSK modulation was then applied reducing the message size to 37509 symbols. A Kasami sequence with spreading factor of 2 was applied (in symbol domain) to each message resulting in 37509 chips per message. A sequence 128 PN BPSK pilot symbols were prepended to each chip packet. Also, a sequence of 128 one bits are appended to each message. Finally, the message is upsampled by 2 and filtered with a RRC pulse shaping filter bringing the total number of chips per message to 75530.

The LFM chirp duration was approximately 18 μs and the bandwidth is varied based on the split factor α. The duration and bandwidth were chosen such that the environment was narrowband. A total of 23300 chirp waveforms were transmitted. Further, the target revisit time of the radar node is fixed to $T = 47.5$ milliseconds.

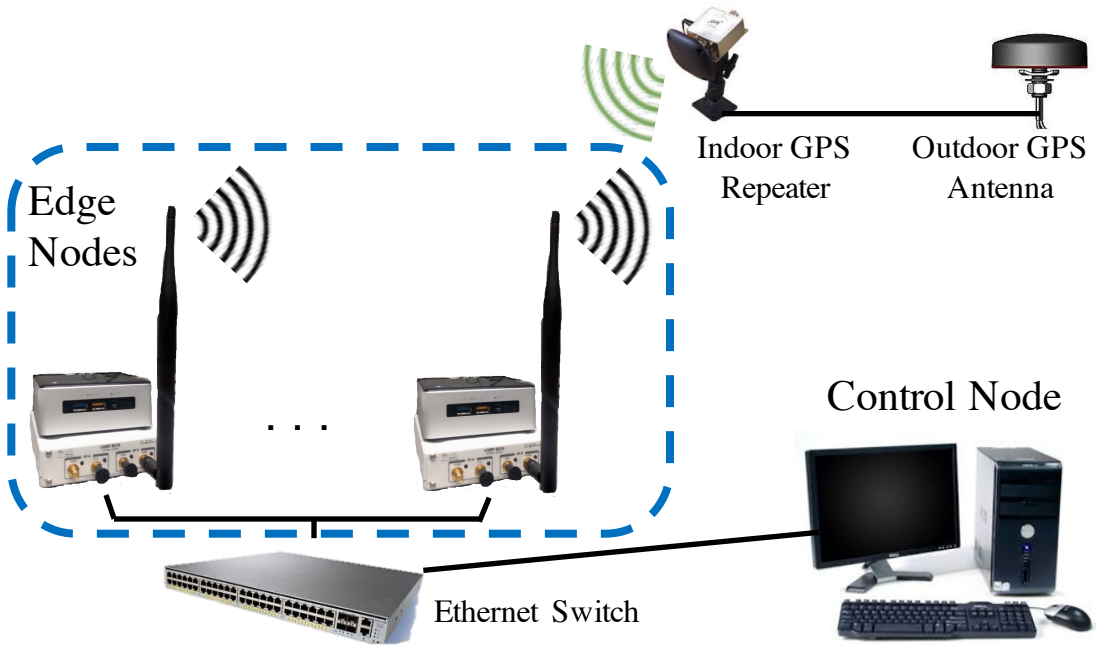

Figure 5.6: Concept of operations for the WISCA SDR Network. The network consists of distributed transceivers connected via ethernet from a control node. The control node distributes a user's MATLAB® code to a specified number of transceivers (edge nodes) which then execute the code on over-the-air data. Each node in the network is synchronized by a GPS reference signal broadcast from a GPS repeater connected to a GPS antenna located outdoors.

A scenario is considered where a target moves along a circular path of diameter 150 m centered at a fixed distance of 5 km from both the radar transmitter and joint radar and communications receiver. Additionally, the target is assumed to move with a constant velocity of 100 m/s. The true target range and range-rate states are generated via the equations for uniform circular motion [82]

$$\begin{bmatrix} R \\ \dot{R} \end{bmatrix} = \begin{bmatrix} R_0 \\ 0 \end{bmatrix} + \begin{bmatrix} \cos(\omega\, n) + \sin(\omega\, n) & 0 \\ 0 & \cos(\omega\, n) - \sin(\omega\, n) \end{bmatrix} \begin{bmatrix} r \\ v \end{bmatrix} \tag{5.5}$$

where $\omega = v/r$ is the angular velocity, r denotes the radius of the circular path, v denotes the constant linear velocity of the target, and R_0 denotes the fixed offset distance of the target from the receiver. These states are then encoded into the LFM chirp waveform as described in Equations (5.2) to (5.4).

The initial state vector is drawn from a Gaussian distribution $\mathbf{x}_0 \sim \mathcal{N}(\mathbf{m}_0, \mathbf{P}_0)$ where mean, $\mathbf{m}_0$, and covariance $\mathbf{P}_0$ are set using estimates obtained during the radar search mode[1]. The receiver also initializes the measurement and process covariance matrices $\mathbf{R}_0$ and $\mathbf{Q}_0$, and then adaptively updates these estimates by utilizing the Kalman filtering algorithm discussed in Section 4.1.3. We summarize the values used in each experiment to initialize Kalman filter below:

$$\mathbf{R}_0 = \begin{bmatrix} 1 & 0 \\ 0 & 1 \end{bmatrix}, \ \mathbf{P}_0 = \begin{bmatrix} 1000 & 0 \\ 0 & 50 \end{bmatrix}, \tag{5.6}$$
$$\mathbf{Q}_0 = \begin{bmatrix} 3.6 \times 10^{-5} & 1.1 \times 10^{-3} \\ 1.1 \times 10^{-3} & 47.5 \times 10^{-3} \end{bmatrix}.$$

The environment was relatively clutter free, other than the interference introduced by the communications waveform, thus the emulated radar return is corrupted mostly by thermal noise. The joint radar and communications node processes one complete coherent processing interval (CPI) of radar waveform and one packet of the communications waveform simultaneously.

Three Ettus Research$^{\text{TM}}$ USRP B-210 transceiver radio nodes were utilized to implement the joint multiple access system topology. Each node was equipped with a vertically polarized (824 - 960 MHz and 1710 - 1990 MHz) quad-band cellular/PCS and ISM band omni-directional 3 dBi antenna. Further, each node was tuned to 900 MHz carrier frequency with 20 MSPS complex sampling rate and each radio node was synchronized via GPS. The communications and radar transmitter gains were set to 50 dB. The joint sensing and communications receiver gain was set to 40 dB. A summary of the experimental USRP B-210 parameters is presented in Table 5.1.

[1]Search mode operation is mimicked by adding Gaussian random noise to the initial true track position.

Table 5.1: Joint Multiple Access System Topology Experimental Parameters

Target Parameters	
v - Linear velocity	100 m/s
r - Path Radius	150 m
R_0 - Initial radial distance	5000 m
q_k - Target process noise	$\{50, 25\}$
Radar Parameters	
f_{pulse} - Pulse repetition frequency	10 kHz
D - Pulse duty cycle	0.3
K - Coherent processing interval	64
T - Target revisit time	47.5 ms
Communications Parameters	
Modulation	Encoded QPSK
R_{sym} - Symbol rate	1/2
K_{SF} - Spreading factor	2
N_{msg} - Total Message Bits	15×10^3
Waveform Amplitude	$A = \{0.6, 0.8\}$
USRP B-210 Parameters	
f_{c} - Carrier frequency	900 MHz
f_{s} - DAC sampling rate	20 MSPS
B_{FIR} - Onboard FIR filter bandwidth	35 MHz
Antenna Gain	3 dBi
UHD TX Gain	50 dB
UHD RX Gain	40 dB
Onboard FIR filter bandwidth	20 MHz

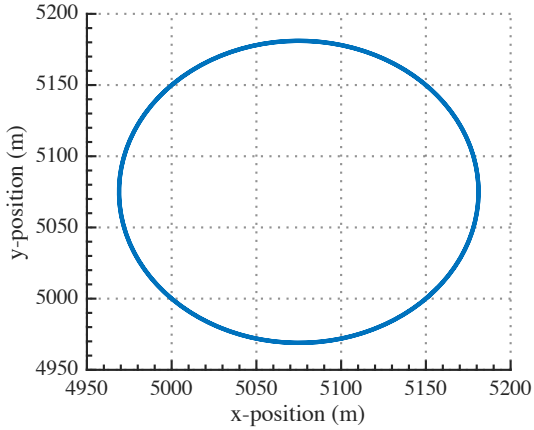

Figure 5.7: The two dimensional target path considered in this work. The radar location (not shown) is set at $x = 0$ and $y = 0$. The initial start point for each path is 5 km (radial distance) away from the radar position. The target moves in a circular path of radius 150 m with a constant velocity of 100 m/s

5.2 Experimental Results

In Section 5.2, the multiple access channel (MAC) bound, SIC operating point, the isolated sub-band (ISB) bound, and the communications water-filling (WF) bound are generated. These bounds are generated by computing the average communications and estimate rate over 200 radar and communications waveform pulses. For each communications waveform pulse, 100 radar waveform pulses are transmitted. The blending ratio α for the experiments are approximate and referenced to 18 MHz of the 20 MHz receiver bandwidth to allow for filter rolloff at the edges. Finally, two communications waveform amplitude values $A = \{0.6, 0.8\}$ and process noise intensities $q_k = \{25, 50\}$ are considered to examine the impact on the ISB and communications WF performance bounds.

5.2.1 Experimental Performance Metrics

The communications rate for each pulse is the ratio of non-redundant to redundant information successfully decoded at the receiver:

$$R_{\text{com}} = \frac{f_{\text{s}}\, N_{\text{bits}}}{N_{\text{enc}}\, R_{\text{sym}}\, K_{\text{SF}}\, L_{\text{up}}}, \tag{5.7}$$

where $N_{\text{bits}} \in \{0, \ldots, N_{\text{msg}}\}$ denotes the number of message bits that the receiver correctly decodes, R_{sym} denotes the symbol rate, L_{up} denotes the upsampling factor of the pulse shaping filter, and N_{enc} denotes the number of encoded bits. The communications rate can be altered by adjusting the number of message bits (N_{bits}), spreading factor (K_{SF}) of the Kasami sequence, or the upsampling factor (L_{up}). The estimation rate for each pulse is computed via Equation (3.15) using the Kalman filter estimates of the measurement prediction covariance ($\mathbf{S}_k$) and measurement noise covariance ($\mathbf{R}_k$). The experimental bounds are shown in Figure 5.9.

5.2.2 Multiple Access Channel Bound

The multiple access channel bound is generated by calculating the communications channel capacity in Equation (5.7) with no radar operation, and computing the experimental radar estimation rate without communications transmitter operation. The horizontal and vertical intersection of these two points represent the best case, yet unachievable, performance for a mixed use channel. The average measured communications rate was approximately 4.4 Mbits/s for the communications only scenario, which is approximately half of the theoretical communications rate. The average measured estimation rate was approximately 27 bits/s for the radar only scenario.

For reference, the theoretical communications rate in Equation (3.4) is also reported. The receiver estimates the instantaneous receive SNR via

$$\text{SNR} \approx \frac{\mathbf{z}_\text{t}\,\mathbf{P}_\mathbf{s}\,\mathbf{z}_\text{t}^\dagger}{\mathbf{z}_\text{t}\,\mathbf{z}_\text{t}^\dagger - \mathbf{z}_\text{t}\,\mathbf{P}_\text{s}\,\mathbf{z}_\text{t}^\dagger}, \tag{5.8}$$

$$\mathbf{P}_\mathbf{s} = \mathbf{S}^\dagger\,(\mathbf{S}\,\mathbf{S}^\dagger)^{-1}\,\mathbf{S} \tag{5.9}$$

$$\mathbf{S} = \begin{bmatrix} \mathbf{s}(\delta_0) & \mathbf{s}(\delta_1) & \ldots & \mathbf{s}(\delta_{\text{L-1}}) \end{bmatrix}^T, \tag{5.10}$$

where ^{T} denotes the non-Hermitian transpose, $\mathbf{P}_\mathbf{s}$ denotes the orthogonal projection of matrix $\mathbf{S}$, and $\mathbf{z}_\text{t} \in \mathbb{C}^{1\times N_\text{t}}$ denotes the N_t received training symbols. The rows of matrix $\mathbf{S} \in \mathbb{C}^{L\times N}$ consist of known training symbols at delays $\{\delta_0, \delta_1, \ldots, \delta_{L-1}\}$. The measured communications rate operates well below the theoretical rate due to the limited number of bits used in the message. This gap can be bridged by encoding a longer message bit stream, which increases the amount of non-redundant information sent over the channel. However, doing this also increases the buffer size needed to process the waveform.

5.2.3 SIC Operating Point

The SIC operating point is generated by computing the estimation and communication rates while the radar and communications nodes are operating in the same spectrum at the same time. The relative bandwidth of each waveform is 18 MHz. The average communications rate decreases (compared to the communications only scenario) to approximately 2.6 Mbits/s for $A = 0.6$ and $q_0 = 50$ and 2.9 Mbits/s for $A = 0.8$ and $q_0 = 25$. This decrease occurs because residual power from radar suppression is large enough to introduce some errors in the communications waveform decoding process, which degrades the communications channel estimate.

The estimation rate remained the same as when the radar operates in isolation. Even with the residual power from the communications waveform present, the ISNR

of the radar waveform was large enough for the Kalman filter to produce accurate estimates. To get a sense of the Kalman filter performance within the mixed environment, a plot the true range and range-rate for the circular target path along with the associated measurements and Kalman filter predictions is presented in Figure 5.10.

Overall, the Kalman filter tracks the range and range-rate of the targets very well. The step like structure in the range estimates occurs as a result of the rounding operation of Equation (5.4) during the the radar target emulation process. Note that these tracks were generated using a wide spread in the initial prediction covariance, $\mathbf{P}_0$, as a result errors in early tracks are larger. The amount of spread in the prediction covariance affects the amount of time it takes the Kalman filter to adapt, and thus affects the estimation rate.

5.2.4 Isolated Sub-Band and Communications Water-Filling

To generate the ISB and communications WF bounds, the bandwidth is split by applying a complex phase ramp to shift the waveforms off of the 900 Mhz carrier frequency of both transmitters. In the ISB case one sub-band is communications only and the other is radar only. In the communications WF case, one sub-band is communications-only and the other is mixed use.

In the experiments, blending ratios of $\alpha \approx \{0, 0.2, 0.5, 1\}$ were considered, where α denotes the relative portion of the bandwidth allocated to the communications waveform and $1 - \alpha$ denotes the relative portion allocated to the radar waveform. These values are approximate due to the inexact nature of the pulse shaping filter. In the communications WF case, the communications transmitter sends two messages containing 7.5×10^3 message bits in each band when a mixed-use sub-band is utilized. The communications rate is computed by summing the average respective rates in each band, that is $R_{\text{ISB,WF}} = R_1 + R_2$, where R_1 and R_2 denote the rates for first and

Table 5.2: Performance Summary of ISB and WF for (a) $A = 0.6$ and $q_0 = 50$ and (b) $A = 0.8$ and $q_0 = 25$.

Split Factor (α)	Communications Rate (Mbits/s)		Estimation Rate (bits/s)	
	ISB	WF	ISB	WF
0	0	2.6	27	27
0.2	1	3	25.2	24.6
0.5	2	3.3	22.5	21.3
1	4.4	4.4	0	0

(a)

Split Factor (α)	Communications Rate (Mbits/s)		Estimation Rate (bits/s)	
	ISB	WF	ISB	WF
0	0	2.9	27	27
0.2	1.8	3.5	26.2	25.8
0.5	2.5	3.8	23.5	23.2
1	4.4	4.4	0	0

(b)

second sub-band. The blending ratios and corresponding average communications and estimation rates for the different parameter sets are summarized in Table 5.2.

The system achieves a maximum communications rate of 4.4 Mbits/s for both the ISB and WF implementations with $\alpha \approx 1$. As α is decreased the amount of bandwidth allocated to radar operation is increased. As a result, an increase in estimation rate is

observed because the radar is able to produce more stable and accurate measurements due to higher ISNR.

A maximum estimation rate of 27 bits/s was observed for both the ISB and WF implementations. However, the best joint performance occurs in the WF implementation because we are able to utilize the entire allocated bandwidth efficiently for both radar and communications.

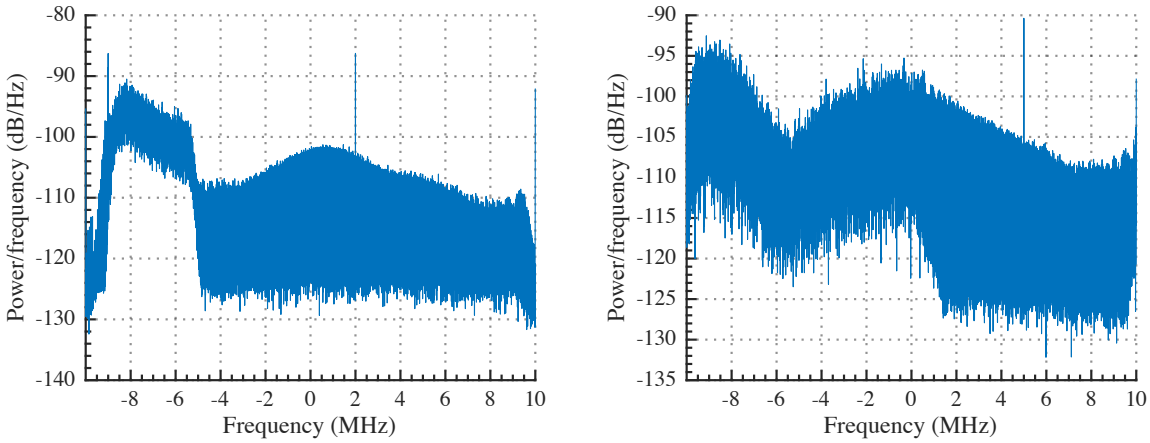

(a) $\alpha = 0.2$

(b) $\alpha = 0.5$

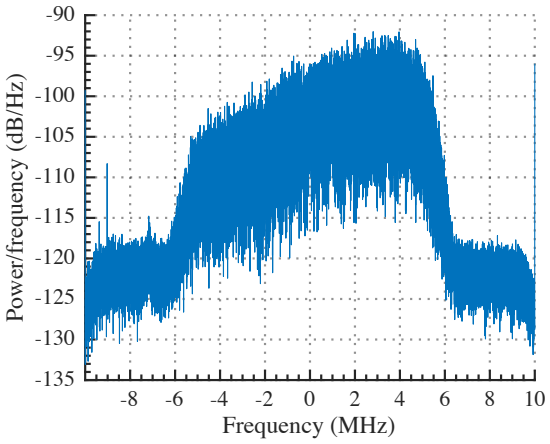

(c)

Figure 5.8: Received spectrum for ISB and communications WF system for different α values. For the ISB system (a) $\alpha \approx 0.2$ the communications bandwidth is reduced enabling more bandwidth to be allocated to radar operation. For the ISB system in (b) $\alpha \approx 0.5$ the bandwidth allocations for both radar and communications are the same. For communications WF system (c) $\alpha \approx 1$ the the entire bandwidth is utilized for mixed use.

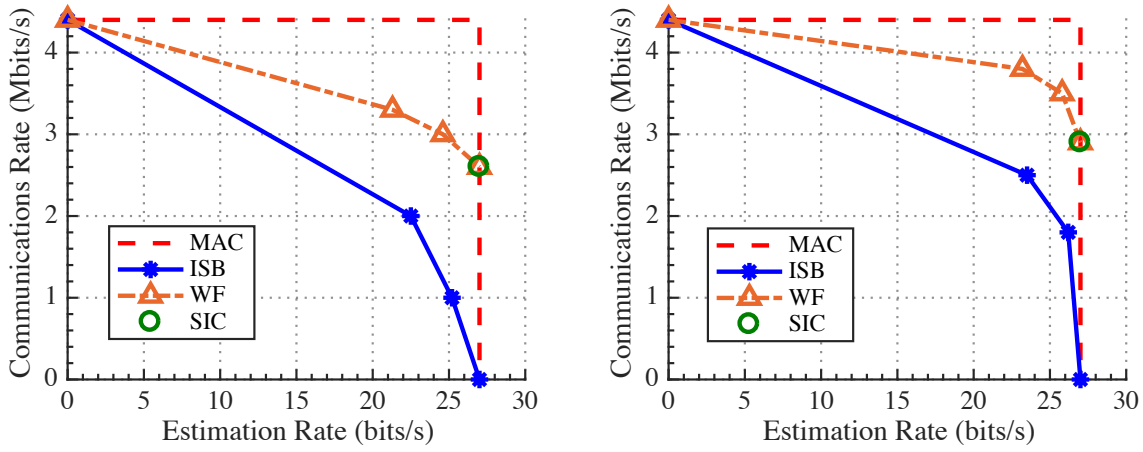

Figure 5.9: Average experimental bounds on joint sensing and communications performance for (a) $A = 0.6$ and $q_k = 50$ and (b) $A = 0.8$ and $q_k = 25$. The points plotted above are calculated by averaging over 200 communications and estimation rate values. Each implementation considered operates below the theoretical communications rate — calculated from SNR estimates at the receiver. For the isolated sub-band (ISB) and water-filling (WF) implementations, blending ratios of $\alpha \approx \{0, 0.2, 0.5, 1\}$ are used. The communications WF approach achieves the best overall joint performance because the entire bandwidth is utilized for both communications and radar. As the communications waveform amplitude is increased a corresponding increase in communications rate is observed. A similar effect is observed for the estimation rate when the process noise is decreased.

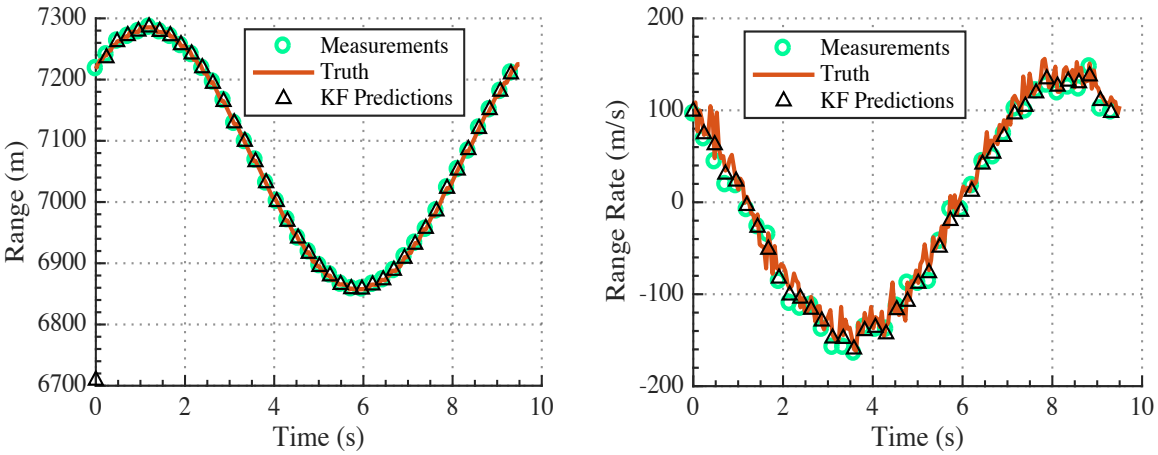

Figure 5.10: (b) Comparison of Kalman filter predictions, range/range-rate estimates, and true range/range-rate values for the emulated target path.

Chapter 6

SUMMARY

In this work significant background and analysis of the UAS-to-ground communications channel was presented. Models were developed for residential and mountainous desert environments using empirical data. In each scenario, a small consumer grade UAS (< 20 kg) flying at an altitude of less than 130 meters transmitted a quadrature phase-shift keying (QPSK) modulated waveform. A stationary basestation was used to capture the transmitted data. The UAS transmitter as well as the receiver base station utilized software defined radio (SDR) technology.The Kullback-Leibler divergence measure was employed to validate the models. Using this measure, the models were determined to provide a good representation of the underlying root mean square (RMS) delay spread probability and cumulative distributions.

In addition to the UAS-to-ground communications channel, significant background and analysis of joint sensing and communications system architectures were discussed. In particular, co-design architectures for the joint multiple access system, isolated subband (ISB) system, and communications waterfilling (WF) system were presented. Each architecture was implemented using a suite of networked SDRs and the system performance was analyzed.

In the experiments, two nodes functioned as independent radar and communications transmitters. The third node functioned as a joint sensing and communications receiver that simultaneously processed the independent waveforms emitted from the transmitters. The performance of each system was characterized using the communications rate capacity and estimation information rate metrics. Further, bounds on the

performance were examined and the feasibility of the algorithms used in constructing a joint multiple access receiver were demonstrated.

6.1 Future Work

6.1.1 UAS Air-to-Ground Wireless Channel Modeling

There are a number of future directions that this work can go. One direction is to characterize and model the UAS air-to-ground channel in more environments. A more dense urban-like area is a prime candidate for collecting new measurements. As well as, some over water environments.

Another avenue of future work is to improve some of the measurement instrumentation on the UAS. For example, a more reliable GPS source will be included in future measurement campaigns. The drop outs in the iPhone GPS measurements made it difficult to provide a more detailed path-loss analysis. Further investigation will be done to determine cause of the large variance from the linear fit.

Finally, future measurement and modeling should incorporate more frequency ranges. These results can then be compared to the models presented in this work. A mobile base station can also be including in further characterizations of the UAS air-to-ground channel.

6.1.2 Joint Sensing and Communications Architectures

The intention of this work was to provide a proof of concept demonstration of various co-design architectures, as well as characterize its performance via over-the-air experiments. The structure of the architectures provide researchers with a template for constructing and gauging the performance of new joint sensing and communication systems. Further, the architecture lends itself well to modification and improvement based on the specific user's needs.

While this early demonstration shows significant promise, we do acknowledge that this work has limitations. In particular, the experiments were carried out in laboratory conditions which does not exhibit the type of dispersion seen in real-world channels. Further, the target response emulation method and assumptions made about the target are often atypical of what is observed in real-world tracking scenarios.

The plan is to address these issues in future work. Furthermore, we plan to explore more complex network topologies, as well as improve upon the robustness of the algorithms.

REFERENCES

[1] Y. Zeng, R. Zhang, and T. J. Lim, "Wireless communications with unmanned aerial vehicles: opportunities and challenges," *IEEE Communications Magazine*, vol. 54, no. 5, pp. 36–42, May 2016.

[2] A. R. Chiriyath, B. Paul, and D. W. Bliss, "Radar-communications convergence: coexistence, cooperation, and co-design," *IEEE Transactions on Cognitive Communications and Networking*, vol. 3, no. 1, pp. 1–12, February 2017.

[3] B. Paul, A. R. Chiriyath, and D. W. Bliss, "Survey of RF communications and sensing convergence research," *IEEE Access*, vol. 5, no. 1, pp. 252–270, December 2016.

[4] W. Tuttlebee, *Software Defined Radio: Enabling Technologies*, ser. Wiley Series in Software Radio. Wiley, 2002.

[5] S. S. T. Group, "New research lab leads to unique radio receiver," E-Systems, Tech. Rep. 4, May 1985.

[6] R. I. Lackey and D. W. Upmal, "Speakeasy: the military software radio," *IEEE Communications Magazine*, vol. 33, no. 5, pp. 56–61, May 1995.

[7] J. Mitola, "Software radios-survey, critical evaluation and future directions," in *[Proceedings] NTC-92: National Telesystems Conference*, May 1992, pp. 13/15–13/23.

[8] G. Dyer, T. G. Gilbert, S. Henriksen, and E. Sayadian, "Mobile propagation measurements using cw and sliding correlator techniques," in *IEEE Antennas and Propagation Society International Symposium. 1998 Digest. Antennas: Gateways to the Global Network. Held in conjunction with: USNC/URSI National Radio Science Meeting (Cat. No.98CH36*, vol. 4, June 1998, pp. 1896–1899 vol.4.

[9] C.-M. Cheng, P.-H. Hsiao, H. Kung, and D. Vlah, "Performance measurement of 802.11a wireless links from uav to ground nodes with various antenna orientations," in *Computer Communications and Networks, 2006. ICCCN 2006. Proceedings.15th International Conference on*, Oct 2006, pp. 303–308.

[10] D. Hague, H. Kung, and B. Suter, "Field experimentation of cots-based uav networking," in *Military Communications Conference, 2006. MILCOM 2006. IEEE*, Oct 2006, pp. 1–7.

[11] E. Yanmaz, R. Kuschnig, and C. Bettstetter, "Channel measurements over 802.11a-based uav-to-ground links," in *GLOBECOM Workshops (GC Wkshps), 2011 IEEE*, Dec 2011, pp. 1280–1284.

[12] W. Khawaja, I. Guvenc, and D. Matolak, "Uwb channel sounding and modeling for uav air-to-ground propagation channels," in *2016 IEEE Global Communications Conference (GLOBECOM)*, Dec 2016, pp. 1–7.

[13] X. Cai, A. Gonzalez-Plaza, D. Alonso, L. Zhang, C. B. Rodríguez, A. P. Yuste, and X. Yin, "Low altitude uav propagation channel modelling," in *2017 11th European Conference on Antennas and Propagation (EUCAP)*, March 2017, pp. 1443–1447.

[14] Z. Qiu, X. Chu, C. Calvo-Ramirez, C. Briso, and X. Yin, "Low altitude uav air-to-ground channel measurement and modeling in semiurban environments," *Wireless Communications and Mobile Computing*, vol. 2017, 2017.

[15] R. M. Gutierrez, D. W. Bliss, H. Yu, and Y. Rong, "Time and frequency dispersion characteristics of the uas wireless channel in residential and mountainous desert terrains," in *14th Annual IEEE Consumer Communications & Networking Conference (CCNC 2017)*, Las Vegas, USA, Jan. 2017.

[16] A. Herschfelt, C. R. Birtcher, R. M. Gutierrez, Y. Rong, H. Yu, C. A. Balanis, and D. W. Bliss, "Consumer-grade drone radar cross-section and micro-doppler phenomenology," in *2017 IEEE Radar Conference (RadarConf)*, May 2017, pp. 0981–0985.

[17] C. Sturm and W. Wiesbeck, "Waveform design and signal processing aspects for fusion of wireless communications and radar sensing," *Proceedings of the IEEE*, vol. 99, no. 7, pp. 1236–1259, July 2011.

[18] A. Turlapaty, Y. Jin, and Y. Xu, "Range and velocity estimation of radar targets by weighted OFDM modulation," in *IEEE Radar Conference*, May 2014, pp. 1358–1362.

[19] S. C. Thompson and J. P. Stralka, "Constant envelope OFDM for power-efficient radar and data communications," in *International Waveform Diversity and Design Conference*, February 2009, pp. 291–295.

[20] G. Hakobyan and B. Yang, "A novel OFDM-MIMO radar with non-equidistant subcarrier interleaving and compressed sensing," in *17th International Radar Symposium (IRS)*, May 2016, pp. 1–5.

[21] X. Shaojian, C. Bing, and Z. Ping, "Radar-communication integration based on DSSS techniques," in *8th International Conference on Signal Processing*, vol. 4, November 2006, pp. 1–4.

[22] Y. Xie, R. Tao, and T. Wang, "Method of waveform design for radar and communication integrated system based on CSS," in *First International Conference on Instrumentation, Measurement, Computer, Communication and Control*, October 2011, pp. 737–739.

[23] M. Roberton and E. R. Brown, "Integrated radar and communications based on chirped spread-spectrum techniques," in *2003 IEEE MTT-S International Microwave Symposium Digest*, vol. 1, June 2003, pp. 611–614.

[24] A. Khawar, A. Abdel-Hadi, and T. C. Clancy, "MIMO radar waveform design for coexistence with cellular systems," in *IEEE International Symposium on Dynamic Spectrum Access Networks (DYSPAN)*, April 2014, pp. 20–26.

[25] Y. L. Sit and T. Zwick, "MIMO OFDM radar with communication and interference cancellation features," in *IEEE Radar Conference*, May 2014, pp. 265–268.

[26] B. Li, A. P. Petropulu, and W. Trappe, "Optimum co-design for spectrum sharing between matrix completion based MIMO radars and a MIMO communication system," *IEEE Transactions on Signal Processing*, vol. 64, no. 17, pp. 4562–4575, May 2016.

[27] Y. Zhang, Q. Li, L. Huang, and J. Song, "Waveform design for joint radar-communication system with multi-user based on MIMO radar," in *2017 IEEE Radar Conference (RadarConf)*, May 2017, pp. 0415–0418.

[28] A. Aubry, V. Carotenuto, A. D. Maio, A. Farina, and L. Pallotta, "Optimization theory-based radar waveform design for spectrally dense environments," *IEEE Aerospace and Electronic Systems Magazine*, vol. 31, no. 12, pp. 14–25, December 2016.

[29] Y. Huang, M. Piezzo, V. Carotenuto, and A. D. Maio, "Radar waveform design under similarity, bandwidth priority, and spectral coexistence constraints," in *2017 IEEE Radar Conference (RadarConf)*, May 2017, pp. 1142–1147.

[30] A. Aubry, V. Carotenuto, and A. D. Maio, "Radar waveform design with multiple spectral compatibility constraints," in *2016 IEEE Radar Conference (RadarConf)*, May 2016, pp. 1–6.

[31] A. Khawar, A. Abdel-Hadi, and T. C. Clancy, "Spectrum sharing between S-band radar and LTE cellular system: A spatial approach," in *IEEE International Symposium on Dynamic Spectrum Access Networks (DYSPAN)*, April 2014, pp. 7–14.

[32] S. Sodagari, A. Khawar, T. C. Clancy, and R. McGwier, "A projection based approach for radar and telecommunication systems coexistence," in *IEEE Global Communications Conference (GLOBECOM)*, Decemeber 2012, pp. 5010–5014.

[33] H. Shajaiah, A. Abdelhadi, and C. Clancy, "Spectrum sharing approach between radar and communication systems and its impact on radar's detectable target parameters," in *IEEE 81st Vehicular Technology Conference (VTC Spring)*, May 2015, pp. 1–6.

[34] W. Zhang, S. Vedantam, and U. Mitra, "Joint transmission and state estimation: A constrained channel coding approach," *IEEE Transactions on Information Theory*, vol. 57, no. 10, pp. 7084–7095, October 2011.

[35] S. Howard, W. Moran, A. Calderbank, H. Schmitt, and C. Savage, "Channel parameters estimation for cognitive radar systems," in *Proceedings IEEE International Conference on Acoustics, Speech, and Signal Processing*, vol. 5, March 2005, pp. 897–900.

[36] B. Li and A. Petropulu, "MIMO radar and communication spectrum sharing with clutter mitigation," in *2016 IEEE Radar Conference (RadarConf)*, May 2016, pp. 1–6.

[37] C. Shannon, "A mathematical theory of communication," *Bell System Technical Journal*, vol. 27, pp. 379–423, 623–656, July, October 1948.

[38] D. W. Bliss, "Cooperative radar and communications signaling: The estimation and information theory odd couple," in *Radar Conference, 2014 IEEE*. IEEE, 2014, pp. 0050–0055.

[39] B. Paul and D. W. Bliss, "Extending joint radar-communications bounds for FMCW radar with Doppler estimation," in *IEEE Radar Conference*, May 2015, pp. 89–94.

[40] B. Paul, A. R. Chiriyath, and D. W. Bliss, "Joint communications and radar performance bounds under continuous waveform optimization: The waveform awakens," in *IEEE Radar Conference*, May 2016, pp. 865–870.

[41] A. R. Chiriyath, B. Paul, and D. W. Bliss, "Joint radar-communications information bounds with clutter: The phase noise menace," in *IEEE Radar Conference*, May 2016, pp. 690–695.

[42] D. W. B. Yu Rong, Alex Chiriyath, "Mulit-antenna multi-access joint radar and communications systems performance bounds," to appear in *Proc. 51st Asilomar Conference on Signals, Systems, and Computers*, 2017.

[43] H. Yu, H. Lee, R. M. Gutierrez, A. Herschfelt, and D. W. Bliss, "WISCA SDR network," in *Milcom 2017 Track 4 - System Perspectives (Milcom 2017 Track 4)*, Baltimore, USA, Oct. 2017.

[44] R. M. Gutierrez, A. Herschfelt, H. Yu, and D. W. Bliss, "Joint radar-communications system implementation using software defined radios: Feasibility and results," to appear in *Proc. 51st Asilomar Conference on Signals, Systems, and Computers*, 2017.

[45] R. M. Gutierrez, H. Yu, A. R. Chiriyath, G. Gubash, A. Herschfelt, and D. W. Bliss, "Assessing joint radar-communications performance bounds using software defined radio," submitted to *IEEE Radar Conference*, April 2018.

[46] D. Bliss and S. Govindasamy, *Adaptive Wireless Communications: MIMO Channels and Networks*. Cambridge University Press, 2013. [Online]. Available: https://books.google.com/books?id=0Ww3zpUKHsYC

[47] D. K. Pradhan and M. Chatterjee, "Glfsr-a new test pattern generator for built-in-self-test," *IEEE Transactions on Computer-Aided Design of Integrated Circuits and Systems*, vol. 18, no. 2, pp. 238–247, Feb 1999.

[48] D. W. Bliss and S. Govindasamy, *Adaptive Wireless Communications: MIMO Channels and Networks*. New York, New York: Cambridge University Press, 2013.

[49] A. Goldsmith, *Wireless Communications*. Cambridge University Press, 2005.

[50] P. Bello, "Characterization of randomly time-variant linear channels," *Communications Systems, IEEE Transactions on*, vol. 11, no. 4, pp. 360–393, December 1963.

[51] I. G. A. Gehring, M. Steinbauer and M. Grigat, "Empirical channel stationarity in urban environments," in *Proc. 4th European Personal Mobile Communications Conf.*, Feb. 2001, pp. 1–6.

[52] G. L. Turin, F. D. Clapp, T. L. Johnston, S. B. Fine, and D. Lavry, "A statistical model of urban multipath propagation," *IEEE Transactions on Vehicular Technology*, vol. 21, no. 1, pp. 1–9, Feb 1972.

[53] G. L. Stüber, *Principles of Mobile Communication*, 3rd ed. Springer Publishing Company, Incorporated, 2011.

[54] D. Tse and P. Viswanath, *Fundamentals of Wireless Communication*, ser. Wiley series in telecommunications. Cambridge University Press, 2005.

[55] S. Stein, "Algorithms for ambiguity function processing," *Acoustics, Speech and Signal Processing, IEEE Transactions on*, vol. 29, no. 3, pp. 588–599, Jun 1981.

[56] A. Molisch, *Wireless Communications*. Wiley India Pvt. Limited, 2007.

[57] J. I. Smith, "A computer generated multipath fading simulation for mobile radio," *IEEE Transactions on Vehicular Technology*, vol. 24, no. 3, pp. 39–40, Aug 1975.

[58] A. Papoulis and S. Pillai, *Probability, Random Variables, and Stochastic Processes*, ser. McGraw-Hill series in electrical engineering: Communications and signal processing. Tata McGraw-Hill, 2002. [Online]. Available: https://books.google.com/books?id=g6eUoWOlcQMC

[59] J. G. Metcalf, K. J. Sangston, M. Rangaswamy, S. D. Blunt, and B. Himed, "A new method of generating multivariate weibull distributed data," in *2016 IEEE Radar Conference (RadarConf)*, May 2016, pp. 1–6.

[60] G. Acosta-Marum and M. A. Ingram, "A ber-based partitioned model for a 2.4ghz vehicle-to-vehicle expressway channel," *Wireless Personal Communications*, vol. 37, no. 3, pp. 421–443, 2006.

[61] C.-D. Iskander and H.-T. Multisystems, "A matlab-based object-oriented approach to multipath fading channel simulation," *Hi-Tek Multisystems*, vol. 21, 2008.

[62] E. Haas, "Aeronautical channel modeling," *IEEE Transactions on Vehicular Technology*, vol. 51, no. 2, pp. 254–264, Mar 2002.

[63] M. Rangaswamy, P. Chakravarthi, D. Weiner, L. Cai, H. Wang, and A. Ozturk, "Signal detection in correlated gaussian and non-gaussian radar clutter," Rome Laboratory, Tech. Rep., 1993.

[64] S. S. Ghassemzadeh, L. J. Greenstein, T. Sveinsson, A. Kavcic, and V. Tarokh, "Uwb delay profile models for residential and commercial indoor environments," *IEEE Transactions on Vehicular Technology*, vol. 54, no. 4, pp. 1235–1244, July 2005.

[65] J. A. Dabin, A. M. Haimovich, and H. Grebel, "A statistical ultra-wideband indoor channel model and the effects of antenna directivity on path loss and multipath propagation," *IEEE Journal on Selected Areas in Communications*, vol. 24, no. 4, pp. 752–758, April 2006.

[66] I. Sen and D. W. Matolak, "Vehicle–vehicle channel models for the 5-ghz band," *IEEE Transactions on Intelligent Transportation Systems*, vol. 9, no. 2, pp. 235–245, June 2008.

[67] S. Kullback and R. A. Leibler, "On information and sufficiency," *Ann. Math. Statist.*, vol. 22, no. 1, pp. 79–86, 03 1951.

[68] D. W. Bliss, "Cooperative radar and communications signaling: The estimation and information theory odd couple," in *IEEE Radar Conference*, May 2014, pp. 50–55.

[69] A. R. Chiriyath and D. W. Bliss, "Joint radar-communications performance bounds: Data versus estimation information rates," in *2015 IEEE Military Communications Conference, MILCOM*, October 2015, pp. 1491–1496.

[70] T. M. Cover and J. A. Thomas, *Elements of Information Theory*, 2nd ed. Hoboken, New Jersey: John Wiley & Sons, 2006.

[71] B. Paul and D. W. Bliss, "Constant information radar for dynamic shared spectrum access," in *2015 49th Asilomar Conference on Signals, Systems and Computers*, November 2015, pp. 1374–1378.

[72] R. E. Kalman *et al.*, "A new approach to linear filtering and prediction problems," *Journal of basic Engineering*, vol. 82, no. 1, pp. 35–45, 1960.

[73] X. R. Li and V. P. Jilkov, "Survey of maneuvering target tracking. part I: Dynamic models," *IEEE Transactions on Aerospace and Electronic Systems*, vol. 39, no. 4, pp. 1333–1364, January 2003.

[74] H. L. Van Trees, *Detection, Estimation, and Modulation Theory: Radar-Sonar Signal Processing and Gaussian Signals in Noise*. Malabar, Florida: Krieger Publishing Company, July 1992.

[75] B. S. Bourgeois, "Using range and range rate for relative navigation," Tech. Rep., September 2007.

[76] B. Paul and D. W. Bliss, "The constant information radar," *Entropy*, vol. 18, no. 9, p. 338, 2016.

[77] A. R. Chiriyath, B. Paul, G. M. Jacyna, and D. W. Bliss, "Inner bounds on performance of radar and communications co-existence," *IEEE Transactions on Signal Processing*, vol. 64, no. 2, pp. 464–474, January 2016.

[78] A. Herschfelt and D. Bliss, "Joint radar-communications waveform multiple access and synthetic aperture radar receiver," to appear in *Proc. 51st Asilomar Conference on Signals, Systems, and Computers*, 2017.

[79] S. Akhlaghi, N. Zhou, and Z. Huang, "Adaptive adjustment of noise covariance in kalman filter for dynamic state estimation," *CoRR*, Jun 2017.

[80] A. Herschfelt and D. Bliss, "Multi-static space-time-frequency multiple access channel simulation and results," in *IEEE Radar Conference*, May 2017, pp. 0975–980.

[81] C. Berrou, A. Glavieux, and P. Thitimajshima, "Near shannon limit error-correcting coding and decoding: Turbo-codes. 1," in *Communications, 1993. ICC '93 Geneva. Technical Program, Conference Record, IEEE International Conference on*, vol. 2, May 1993, pp. 1064–1070 vol.2.

[82] D. Kleppner and R. Kolenkow, *An introduction to mechanics*. Cambridge University Press, 2013.

APPENDIX A

LIST OF ACRONYMS

BPSK binary phase-shift keying

DARPA The Defense Advanced Research Projects Agency

ISB isolated sub-band

LFM linear frequency-modulated

LoS line-of-sight

MAC multiple access channel

OFDM orthogonal frequency-division multiplexing

QPSK quadrature phase-shift keying

RF radio frequency

SDR Software-defined radio

SIC successive interference cancellation

SNR signal-to-noise ratio

UAS unmanned aerial system

WF water-filling

WISCA Center for Wireless Information Systems and Computational Architectures